

2014-01-01

# Strongly Coupled Quark Matter: Chiral Symmetry Breaking in a Magnetic Field, and EoS in the BEC-BEC Crossover

Israel Portillo Vazquez

*University of Texas at El Paso*, [iportillovazquez@me.com](mailto:iportillovazquez@me.com)

Follow this and additional works at: [https://digitalcommons.utep.edu/open\\_etd](https://digitalcommons.utep.edu/open_etd)



Part of the [Computer Sciences Commons](#), and the [Physics Commons](#)

---

## Recommended Citation

Portillo Vazquez, Israel, "Strongly Coupled Quark Matter: Chiral Symmetry Breaking in a Magnetic Field, and EoS in the BEC-BEC Crossover" (2014). *Open Access Theses & Dissertations*. 1328.

[https://digitalcommons.utep.edu/open\\_etd/1328](https://digitalcommons.utep.edu/open_etd/1328)

STRONGLY COUPLED QUARK MATTER:  
CHIRAL SYMMETRY BREAKING IN A MAGNETIC FIELD,  
AND EOS IN THE BCS-BEC CROSSOVER

ISRAEL PORTILLO VAZQUEZ

Computational Science Program

APPROVED:

---

Efrain J. Ferrer, Ph.D., Chair

---

Vivian Incera, Ph.D.

---

Vladik Kreinovich, Ph.D.

---

Bess Sirmon-Taylor, Ph.D.  
Interim Dean of the Graduate School

©Copyright

by

Israel Portillo Vazquez

2014

STRONGLY COUPLED QUARK MATTER:  
CHIRAL SYMMETRY BREAKING IN A MAGNETIC FIELD,  
AND EOS IN THE BCS-BEC CROSSOVER

by

ISRAEL PORTILLO VAZQUEZ, M.S.

THESIS

Presented to the Faculty of the Graduate School of

The University of Texas at El Paso

in Partial Fulfillment

of the Requirements

for the Degree of

DOCTOR OF PHILOSOPHY

Computational Science Program

THE UNIVERSITY OF TEXAS AT EL PASO

August 2014

# Abstract

We explore chiral symmetry breaking in a magnetic field within a Nambu-Jona-Lasinio model of interacting massless quarks including tensor channels. The new interaction channels are opened up through Fierz identities due to the breaking of the rotational symmetry by the magnetic field. We demonstrate that the magnetic catalysis of chiral symmetry breaking leads to the generation of two independent condensates, the conventional chiral condensate and a spin-one condensate. While the chiral condensate generates a dynamical fermion mass, the spin-one condensate gives rise to a dynamical anomalous magnetic moment for the fermions. We also investigate the possibility of a crossover from a BCS to a BEC (Bardeen-Cooper-Schrieffer to Bose-Einstein Condensation) phase for strongly-coupled quark matter, and its implications for the system equation of state. The study uses zero temperature effective quark models at densities beyond nuclear density. We use mean-field approximation and consider quark-quark, quark-antiquark, and diquark-diquark interactions. We determine the region of parameters where the crossover can take place for a stable system (i.e. that with a corresponding positive pressure). To carry out this investigation, we first use a simple relativistic model of one-flavor fermions, and then, we consider a more realistic two-flavor model for strongly interacting quarks

# Table of Contents

	<b>Page</b>
Abstract . . . . .	iv
Table of Contents . . . . .	v
List of Tables . . . . .	vii
List of Figures . . . . .	viii
<b>Chapter</b>	
1 Introduction . . . . .	1
1.1 The QCD Phase Diagram . . . . .	3
1.2 QCD in a Magnetic Field . . . . .	5
1.3 Color Superconductivity and the BCS-BEC Crossover . . . . .	7
2 Anomalous Magnetic Moment of Massless Quarks in a Strong Magnetic Field . .	11
2.1 NJL Model in a Magnetic Field . . . . .	11
2.2 Effective Potential in the Mean-Field Approximation . . . . .	14
2.3 Condensate Solutions . . . . .	18
2.3.1 Gap Equations . . . . .	18
2.3.2 Effect on the Quasiparticle's Effective Mass . . . . .	20
2.4 Critical Temperature . . . . .	21
2.4.1 Condensate Solutions at Finite Temperature . . . . .	21
2.4.2 Critical-Temperature Analytical Expression . . . . .	23
3 The EoS in the BCS-BEC Crossover of a Simple Fermion System . . . . .	25
3.1 Fermion Model . . . . .	25
3.2 Gap and Mass Equations at Fixed Particle Number Density . . . . .	28
3.3 Equation of State Along the BCS-BEC Crossover . . . . .	28
3.4 BCS-BEC Crossover and Critical Values . . . . .	29
4 BCS-BEC Crossover for Strongly Coupled 2CS Matter . . . . .	36

4.1	2SC Model . . . . .	37
4.2	Gap Equation and Neutrality Conditions at Fixed Particle Density . . . . .	40
4.3	Equation of State Along the BCS-BEC Crossover . . . . .	41
4.4	Numerical Results: EoS in the 2SC Phase . . . . .	41
5	Numerical Method . . . . .	48
5.1	Numerical Integration . . . . .	49
5.2	Numerical Differentiation . . . . .	51
5.3	Minimization Method . . . . .	53
5.3.1	Merit Function . . . . .	54
5.3.2	Newton's Method . . . . .	55
5.3.3	Line Search . . . . .	56
5.3.4	Global Strategy . . . . .	57
6	Remarks . . . . .	60
6.1	AMM in Massless Quarks . . . . .	60
6.2	BCS-BEC Crossover . . . . .	61
	References . . . . .	63
	Curriculum Vitae . . . . .	70

# List of Tables

5.1	Gaussian Quadrature Error Estimate . . . . .	51
-----	--	----



# List of Figures

1.1	Schematic QCD Phase Diagram . . . . .	4
2.1	Condensate $\xi$ Vs $T$ . . . . .	23
3.1	Quark Model $\tilde{\mu}$ and $\tilde{P}$ vs $\hat{G}_D$ at $\tilde{P}_F = 0.10$ and $\hat{G}_S = 1.20$ . . . . .	31
3.2	Quark Model $\tilde{\Delta}$ and $\tilde{\varepsilon}$ vs $\hat{G}_D$ at $\tilde{P}_F = 0.10$ and $\hat{G}_S = 1.20$ . . . . .	32
3.3	Quark Model $\tilde{\varepsilon}_k^+$ before and after the crossover . . . . .	33
3.4	Quark Model Stable BCS-BEC Crossover at $\hat{\lambda} = 0$ . . . . .	34
3.5	Quark Model Stable BCS-BEC Crossover at $\hat{\lambda} = 50$ . . . . .	35
4.1	2SC Crossover and Vacuum Mass at $\tilde{G}_S = 2.14$ . . . . .	42
4.2	2SC BCS-BEC $\tilde{\mu}$ and $\tilde{P}$ vs $G_D$ at $\tilde{G}_S = 2.14$ . . . . .	43
4.3	2SC $\Delta$ , and $\mu_{ub}$ and $\mu_{db}$ vs $G_D$ at $\tilde{G}_S = 2.14$ . . . . .	44
4.4	Chemical Potentials $\mu_e$ and $\mu_8$ at $\tilde{G}_S = 2.14$ . . . . .	45
4.5	2SC $\varepsilon$ before and after the BCS-BEC crossover vs $k$ . . . . .	46
4.6	Crossover in the $\tilde{G}_S - \tilde{G}_D$ plane, and $\Delta$ and $m$ , at different $n_F$ . . . . .	47
5.1	Discretization . . . . .	52
5.2	Mesh of Initial Points . . . . .	58

# Chapter 1

## Introduction

Our current understanding of the laws that govern the fundamental particles have been written successfully in the language of quantum field theory (QFT). At high energy, those laws can be summarized in the Standard Model of particles [1]. This model has extended and generalized the quantum theory of electromagnetism (QED) with the weak nuclear forces into a unified Electro-Weak theory. In a similar way, Quantum Chromodynamics (QCD), the theory of quarks and gluons, proves an analogous theory of the strong nuclear forces. Together they summarize our present knowledge of the basic constituent of matter in terms of Abelian and non-Abelian gauge theories based on symmetry groups. Symmetries play a central role in the understanding of modern physics and in the construction of the Standard Model. One important aspect of gauge symmetries is that they can spontaneously be broken and not be manifest in physical observable.

Symmetry breaking was well known in classical physics in the form of phase transitions and had been formalized in the theory of Ginzburg-Landau (GL) [2]. The GL theory, in a statistical context, allows an understanding of the different states of atomic matter. The mechanism that leads to the transitions between different phases can be characterized by an order parameter that describes the symmetry-breaking. In similar way, symmetries can be broken in QFT. For example, in the thermal evolution of the Universe, the electro-weak system starts from a symmetric phase with massless fermions (quarks and leptons) and four massless bosons that carries the electro-weak force. Introducing as order parameter a scalar field, known as the Higgs field, the theory predicts that below a certain energy scale the Higgs will acquires a non-zero vacuum expectation value (vev). The appearance of the Higgs field vev will break the electro-weak symmetry down to the gauge symmetry of elec-

tromagnetism, and three of the force-carried bosons will become massive. The interaction of the particle field with the non-trivial ground state of the Higgs condensate will generate the constituent mass of quarks and leptons.

On the other hand, the theory of strong interactions, QCD, is described with an additional color symmetry group. The immediate implication of this symmetry is that quarks will never be observed in isolation. At energies lower than the so called QCD energy scale ( $\Lambda_{QCD}$ ), the quarks are confined by their strongly interacting gluons to be colorless in group of three forming baryons, or as quark-antiquark pair forming mesons. In addition, at sufficient high energies the theory is invariant under the interchange of left and right handed quarks. This symmetry is known as a chiral symmetry. Increasing the energy scale, the quark current masses can be neglected, and an approximate flavor symmetry emerges. The breaking of those two symmetries give rise to a rich diversity of phases and phenomena. In regard of this, QCD has become a great challenge for both experimentalist and theoreticians. The study of quark matter in extreme environments, such as high temperature  $T$ , high baryon density  $\mu_B$ , strong external fields, etc., is essential to unveil the properties of nuclear matter and for a better understanding of many phenomena in cosmology, astrophysics and heavy ion collision experiments. These probes bring us closer to the ultimate goal of understanding QCD.

This thesis is dedicated to the study of two phenomena within the context of quark matter in the extremes of high temperature, high density and strong magnetic field. In Chapter 2, we explore chiral symmetry in a strong magnetic field for a system of massless fermions. We show that, in addition to a dynamical mass, a dynamical anomalous magnetic moment is generated once the chiral symmetry is broken. In Chapter 3, we investigate the possibility of a crossover from the Bardeen-Cooper-Schrieffer (BCS) superfluidity/superconductivity state to a Bose-Einstein condensation (BEC) one in a simplified model of relativistic quarks. Later in Chapter 4, we explore the possibility of the BCS-BEC crossover in a more realistic model with  $u$  and  $d$  quarks. The strongly-coupled-quark-matter model used is the 2SC. Finally, in Chapter 5, we describe the methods employed to solve the numerical problems

that were presented in Chapter 2-4. And we summarize the main outcomes of our investigation and make our concluding remarks in Chapter 6. The remainder of this chapter is dedicated to a brief introduction to several topics of interest for the present work and to providing a motivation and possible implications of our investigation.

## 1.1 The QCD Phase Diagram

The phases of the low-energy regime of QCD, where only the  $u$ ,  $d$ , and  $s$  quarks may form, are commonly mapped in the plane of temperature  $T$  and baryon-number chemical potential  $\mu$ . This representation is known as the QCD phase diagram. Each phase is characterized by their symmetries and order parameters. The different phase boundaries that have been found are model dependent. They are particularly influenced by the values of the coupling constant, the constituent  $s$  quark mass ( $m_s$ ), and the introduction of external conditions as magnetic field, temperature, etc. However, thanks to the asymptotic freedom of the theory (the nuclear interaction is asymptotically free [3], what means that the strength of the strong force decreases with the energy scale. At high energies the quarks becomes closer and interact weakly), the extremes in the QCD phase diagram have states of matter well described by theoretical models that use the perturbative techniques allowed in those high-energy regions. Fig. 1.1 describes the QCD phase diagram with a simple sketch of the global phases of QCD pointing out the energy regions of the high-energy experiments that has been conducted in the last years [4].

In the high temperature ( $T > \Lambda_{QCD}$ ) and low density asymptote, it is found the quark-gluon plasma (QGP), a state of matter formed by quarks and gluons where there is neither color confinement nor quark dynamical mass. This regime has been successfully analyzed employing lattice QCD calculations [5], and has been the subject of ultra-relativistic heavy-ion colliders. The existence of the QGP phase has been confirmed by the Relativistic Heavy Ion Collider (RHIC) at Brookhaven National Laboratory (BNL) and by the Large Hadron Collider (LHC) at the European Organization for Nuclear Research (CERN). The results

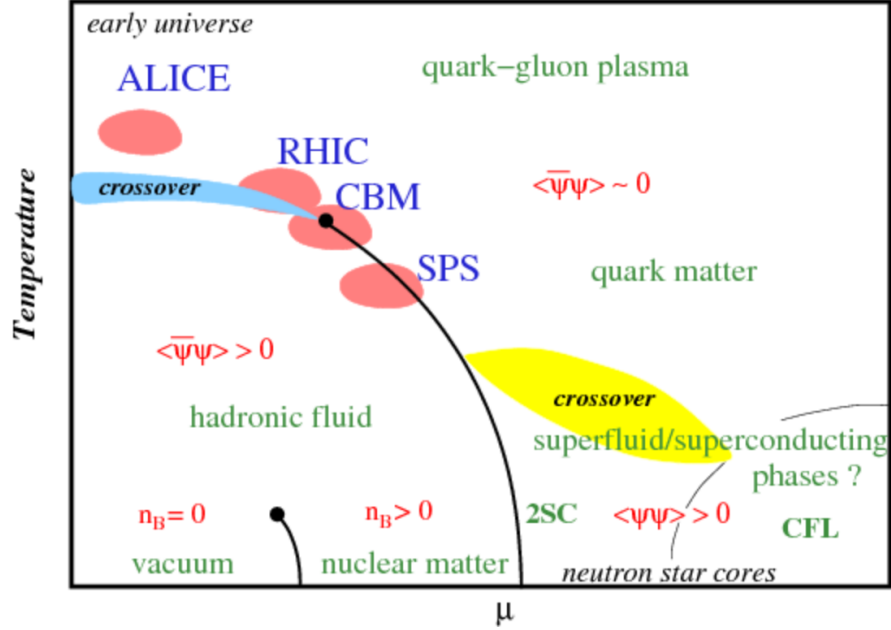


Figure 1.1: Schematic QCD Phase Diagram [4]

of both experiments also confirm the existence of a crossover transition from QGP to a phase of hadrons, at a temperature of approximately 170 MeV.

On the other extreme of high density ( $\mu_B > m_s$ ) and low temperatures, baryonic matter is also deconfined. The dense and weakly interacting quarks are unstable under the formation of Cooper pairs, a phenomenon in QCD similar to the BSC instability in conventional superconductivity, producing a new ground state formed by colored diquark. Here, all three flavors and three colors forms pairs in a more energetic phase known as Color-Flavor-Locked (CFL) [6]. Moving down in density, the CFL phase becomes unstable. A rich spectrum of superconducting phases has been suggested to replace the CFL; however, at present, it is not clear which state is the ultimate one. The problem is that some parameters concerning the superconducting phases, like the quark masses and their couplings, are not accessible to observation at those regimes, and their values rely only on educated guesses. However, the measure of the physical values of the quark masses, as increasing the baryon density at low

temperatures, implies that the chiral symmetry breaking transition, where hadronic matter becomes deconfined-superdense matter, is a first order transition [7]. Consequently in the QCD diagram, there will be a critical point that delimits the crossover from the first order phase transition. The location of this critical point has been addressed by ultra-relativistic heavy-ion experiments, performed at CERN and BNL.

The asymptotic behavior and the transition to the hadronic phase are the most secure parts in the QCD diagram. Nonetheless, part of our investigation is placed in the intermediate region of densities at low temperature. The study of this region is a challenging theoretical problem that, at the moment, cannot be addressed by experiments nor by QCD lattice calculation. However, it is known that the ground state at those regions may have a superconducting condensate formed by the pairing of quarks ( $\langle qq \rangle$ ), and a chiral condensate formed by a pairing of quarks and anti-quarks with opposite spins ( $\langle \bar{q}q \rangle$ ). The first condensate produces a gap in the energy spectrum and the later one produces a dynamical mass. The spontaneous breaking of those two symmetries is usually studied employing effective models of QCD like the Nambu-Jona-Lasinio (NJL) model that although fails to describe confinement, it captures the essences of the symmetry breaking phenomena. This model can be seen as the result of integrating all the gluons in the one gluon exchange, which is a good approximation at high densities, and will be the starting point in our studies.

## 1.2 QCD in a Magnetic Field

Extremely high magnetic fields ( $\sim 10^{18}$  G) [8,9] can be generated in noncentral Au-Au collisions for top collision energies  $\sqrt{S_{NN}} = 200$  GeV at the RHIC at BNL, and even larger fields ( $\sim 10^{19}$  G) can be generated for the energies reachable at the LHC at CERN,  $\sqrt{S_{NN}} = 4.5$  TeV, for the Pb-Pb collisions [9]. Even though these magnetic fields decay quickly, they may influence the properties of the particles generated during the collision. Later in this decade, the Facility for Antiproton and Ion Research (FAIR) at the Society

for Heavy Ion Research (GSI) will open the possibility to explore the intermediate region of temperatures and densities. Strong magnetic fields will likely be also generated at FAIR, making possible to explore the region of higher densities under a magnetic field.

An other physical environment where the influence of a magnetic field in the state of quark matter is relevant is the core of neutron stars, which typically are very magnetized objects reaching surface magnetic fields as large as  $10^{14} - 10^{16}$  G [10]. Moreover, due to the very high electric conductivity, the magnetic flux should be conserved, and it is natural to expect a stronger field strength with increasing matter density at the core. The interior magnetic fields are however not directly accessible to observation. Estimates based on macroscopic and microscopic analysis, considering both gravitationally bound and self-bound stars, have led to maximum fields within the range  $10^{18} - 10^{20}$  G, depending whether the inner medium is formed by neutrons [11] or by quarks [12].

A uniform magnetic field has a strong tendency to enhance fermion-antifermion spin-0 condensate in any charged-fermionic system with arbitrarily weak attractive interaction. This phenomenon is known in the literature as the magnetic catalysis of chiral symmetry breaking (MC $\chi$ SB) [13]. The mechanism responsible for such effect is related to the dimensional reduction of the infrared dynamics of the particles in the lowest Landau level (LLL). Such a reduction favors the formation of a chiral condensate because there is no energy gap between the infrared fermions in the LLL and the antiparticles in the Dirac sea. The MC $\chi$ SB modifies the vacuum properties and induces dynamical parameters that depend on the applied field. This effect has been actively investigated assuming that the catalyzed chiral condensate generates only a fermion dynamical mass [14–18]. However, it has been shown recently that in QED the MC $\chi$ SB leads to a dynamical fermion mass and inevitably also to a dynamical anomalous magnetic moment (AMM) [19]. This is connected to the fact that the AMM does not break any symmetry that has not already been broken by the other condensate. The dynamical AMM in massless QED leads, in turn, to a non-perturbative Lande g-factor and Bohr magneton proportional to the inverse of the dynamical mass. The induction of the AMM also yields a non-perturbative Zeeman effect.

An important aspect of the  $MC\chi SB$  is its universal character, and one expects that the dynamical generation of the AMM should also occur in QCD. Regarding this, Chapter 2 is dedicated to investigate the influence of a magnetic field on the QCD chiral transition in a system of massless fermions. We explore a tensor channel in the one-flavor one-color NJL model that opens up via Fierz identities due to the explicit breaking of the rotational symmetry by the magnetic field. This tensor channel is important only in the presence of a magnetic field, and leads to the generation of two independent condensates. One generates a dynamical mass, while the other generates a dynamical AMM.

### 1.3 Color Superconductivity and the BCS-BEC Crossover

The idea behind the BCS theory of superconductivity is the formation of Cooper pairs. For sufficiently low temperatures, the Cooper pairs will resist temperature fluctuations, producing a condensation that will modify the ground state and break some of the symmetries of the underlying theory. In QCD, the ground state of the superdense quark system, a Fermi liquid of weakly interacting quarks, is unstable with respect to the formation of diquark condensates [20]. This non-perturbative phenomenon is essentially equivalent to the Cooper instability in the BCS theory. The attractive channels are provided by the one gluon exchange color-antitriplet channel. The color condensates break the  $SU(3)$  color gauge symmetry of the ground state producing a color superconductor.

A natural scenario where color superconductivity could be realized is in the interior of compact astrophysical objects as neutron stars. There, matter can reach densities estimated to be several times larger than the nuclear saturation density and temperatures several orders smaller than the superconducting gap. Also, there exists a possibility that color superconductivity could be found in future experiments planned at FAIR at GSI, the Nucleon-Ion Collider Facility (NICA) at the Joint Institute for Nuclear Research (JINR)



in Dubna, and the Japan Proton Accelerator Research Complex (JPARK) at the Japan Atomic Energy Research Institute (JAERI), all of which intend to complement the experiments at RHIC and LHC by reaching regions of even higher densities and intermediate to low temperatures in the QCD phase map.

Nonetheless, in both referred scenarios the color superconducting state will be realized at densities which are not asymptotically high. At these intermediate densities, the CFL phase breaks down due to the mismatch between the Fermi momenta of the heavier  $s$  quark with the light  $u$  and  $d$  quarks, and to the constraints imposed by electric and color neutralities [21]. As a consequence of the pairings with mismatched Fermi surfaces, the CFL phase exhibits chromomagnetic instabilities [22]. To remove such instabilities several interesting proposals exist, e.g. the existence of inhomogeneous condensates [23]; a LOFF phase on which the quarks pair with nonzero total momentum [24]; and an inhomogeneous gluon condensate together with the spontaneous induction of an in medium magnetic field [25]. At present, it is not clear if any of these proposals is the final solution to the instability problem. On the other hand, taking into account the running of the coupling constant with the energy scale, it is expected that in the moderate density region the coupling constant turns stronger. Then, one possible scenario where the chromomagnetic instability can be avoided occurs if in the region of moderate-low densities the strong coupling constant becomes sufficiently high ( $G_D \approx G_S \approx 1/\Lambda^2$ , with  $G_D$  and  $G_S$  denoting the diquark and quark-antiquark coupling constants respectively) [26, 27]. In this situation it was found that the more stable phase at  $T = 0$  is the strongly-coupled 2SC one.

Nevertheless, the increase of the coupling constant strength that occurs at intermediate density can modify the properties of the ground state by decreasing the Cooper-pair coherence length, which can reach values of the order of the inter-quark spacing [28]. As already found in other physical contexts [29], this fact strongly suggests the possibility of a crossover from a BCS superfluidity/superconductivity to a BEC state of composite molecules, where although the symmetry breaking order parameter (the diquark condensate) is the same, the quasiparticle spectra in the two regions are completely different. In the BCS side, the

coherence length of the pairs is much larger than the mean inter-particle distance and as a consequence the fermionic degrees of freedom are still manifested. However, in the BEC state, the fermions pairs are bound into a bosonic molecule and no fermionic degrees of freedom remain. This finding in non-relativistic systems, together with the fact that the diquark BEC phase could be the natural phase reached after deconfinement, strongly suggests the possibility of a crossover from a color-superconducting BCS dynamics to a BEC one in QCD. Several studies in this direction have been already pursued by using different relativistic models and calculational techniques [30–34].

Having in mind that the possible realization of the BCS-BEC crossover can take place in the core of neutron stars, it turns very important to investigate the effect of the formation of the Bose-diquark cluster on the matter pressure, since it should balance the strong gravitational inward pressure at the star’s core. In this context, we should take into account that the ground state of the diquark cluster will be a pressureless zero-momentum Bose condensate. Since for this astrophysical medium we can consider that  $T \ll \mu$ , it should be expected that the system of free diquarks becomes almost pressureless at those relatively low temperatures. However, as it was pointed out in Ref. [35], together with the fact that there exists an attractive channel between quarks that favors the diquark formation, there is also a diquark-diquark repulsion. This repulsion is due to the cross-channel unfavorable correlations between the quarks belonging to different diquarks. Hence, when the diquark repulsion is self-consistently taken into account in the EoS of this system, the instability previously found in the strong coupling region can be removed, stabilizing the pressure. The increase of the diquark repulsion compensates the effect of the decay of the chemical potential, which is known to make an important contribution to the EoS [36].

In this direction, part of our investigation is to analyze whether a BCS-BEC crossover may appear in a realistic model for compact stars. We employ multi-fermion NJL models including the chiral condensate, the diquarks formation, and the diquarks repulsion. The investigation is carried out self-consistently through the mean-field approximation. We map the spectrum of possible parameters where the BCS-BEC crossover may take place, and

its consequences in the system EoS. In this way, we investigate the realization of a stable (i.e. having a positive pressure) BCS-BEC crossover in a wide parameter regime. First in Chapter 4, we want to get an insight of the interplay of both superconducting and chiral condensates in a simple model of fermions. Later in Chapter 5, we consider the strongly coupled 2SC model that, as mentioned before, may be a suitable model for the densities inside compact stars.

# Chapter 2

## Anomalous Magnetic Moment of Massless Quarks in a Strong Magnetic Field

A magnetic field is known to enhance the chiral condensate in many systems of fermions with arbitrarily weak attractive interaction (MC $\chi$ SB). This effect has been actively investigated assuming that the condensate generates only a fermion dynamical mass. Recently, a similar scenario was studied in QED [19]; and it was found that the MC $\chi$ SB leads to a dynamical fermion mass and inevitably also to a dynamical AMM. Similarly, and considering that the MC $\chi$ SB is a universal phenomenon, the purpose of this Chapter is to investigate the dynamical generation of a net magnetic moment in the ground state of QCD and discuss its implications for the chiral phase transition at finite temperature using a NJL model with four-fermion point interactions. The use of NJL models to explore chiral symmetry breaking in QCD with nonzero magnetic field has been a successful strategy followed in many previous works [37, 38]. The new element in the present investigation will be the introduction of a yet unexplored four-fermion channel that becomes relevant only in the presence of a magnetic field and can lead to non-trivial physical consequences [39].

### 2.1 NJL Model in a Magnetic Field

Our main goal here is to investigate the effect of a constant and homogeneous magnetic field in the spontaneous breaking of chiral symmetry for a system of massless quarks. We

use a simple NJL model that can be interpreted as the result of integrating out the gluon fields and quark fluctuations with momenta larger than some scale  $\Lambda$ , with  $\Lambda \gtrsim \Lambda_{QCD}$ . Our NJL model of massless quarks in the presence of a constant and uniform magnetic field is given by the Lagrangian density

$$\mathcal{L} = \bar{\psi}i\gamma^\mu D_\mu\psi + \mathcal{L}_{int}^{(1)} + \mathcal{L}_{int}^{(2)} \quad (2.1)$$

The single-flavor Dirac spinor  $\psi$  belongs to the fundamental representation of the  $SU(N_c)$  color group. The electromagnetic four-potential in the covariant derivative  $D_\mu = \partial_\mu + iqA_\mu^{(ext)}$  is chosen, without loss of generality, in the gauge  $A_\mu^{(ext)} = (0, 0, Bx_1, 0)$ , so to have a constant and homogenous magnetic field of magnitude  $B$  pointing in the  $x_3$ -direction. We use the Lorentz metric  $\eta_{\mu\nu} = (1, -\vec{1})$  and the Dirac matrices in the chiral representation. The interaction

$$\mathcal{L}_{int}^{(1)} = \frac{G}{2} [(\bar{\psi}\psi)^2 + (\bar{\psi}i\gamma^5\psi)^2], \quad (2.2)$$

has the conventional four-fermion scalar and pseudoscalar channels used in many previous studies based on NJL [38]. In addition, we introduce a new channel

$$\mathcal{L}_{int}^{(2)} = \frac{G'}{2} [(\bar{\psi}\Sigma^3\psi)^2 + (\bar{\psi}i\gamma^5\Sigma^3\psi)^2], \quad (2.3)$$

that preserves chiral symmetry and rotations about the magnetic field direction; here  $\Sigma^3 = \frac{i}{2}[\gamma^1, \gamma^2] = \sigma_\perp^{\mu\nu}$  is the spin operator in the direction of the applied field. In Eqs. (2.1)-(2.3), summation over color index has been assumed.

A uniform magnetic field always selects a preferable direction and explicitly breaks the rotational symmetry into a parallel and transverse to the field directions. The new interaction channel  $\mathcal{L}_{int}^{(2)}$  with second-rank tensor structure naturally emerges using the Fierz identities in the one-gluon-exchange channels of QCD when the rotational symmetry is broken. This, in turn, implies that the tensor structures of the Dirac ring split in components parallel and transverse to the field direction with the help of the normalized tensor  $\widehat{F}_{\mu\nu} = F_{\mu\nu}/|B|$ ,

$$\gamma^\parallel = \eta_\parallel^{\mu\nu}\gamma_\nu, \quad \gamma^\perp = \eta_\perp^{\mu\nu}\gamma_\nu \quad (2.4)$$

with

$$\eta_{\parallel}^{\mu\nu} = \eta^{\mu\nu} - \widehat{F}^{\mu\rho}\widehat{F}_{\rho}^{\nu}, \quad \eta_{\perp}^{\mu\nu} = \widehat{F}^{\mu\rho}\widehat{F}_{\rho}^{\nu}. \quad (2.5)$$

being the longitudinal and transverse Minkowskian metric tensors respectively. In the rest frame, for a magnetic field in the  $x_3$  direction,  $\eta_{\parallel}^{\mu\nu}$  has only  $\mu, \nu = 0, 3$  components, and  $\eta_{\perp}^{\mu\nu}$  has  $\mu, \nu = 1, 2$ .

As a consequence, the four-fermion interaction Lagrangian density splits into two terms,

$$\mathcal{L}_{int} = \frac{g_{\parallel}^2}{2\Lambda^2}(\bar{\psi}\gamma_{\parallel}^{\mu}\psi)(\bar{\psi}\gamma_{\mu}^{\parallel}\psi) + \frac{g_{\perp}^2}{2\Lambda^2}(\bar{\psi}\gamma_{\perp}^{\mu}\psi)(\bar{\psi}\gamma_{\mu}^{\perp}\psi). \quad (2.6)$$

Notice that despite the fact that there is no direct coupling between the gluons and the magnetic field, the fermion vertex is modified because of the distinction between longitudinal and transverse fermion modes in this case. The extreme case occurs for magnetic fields of the order of the energy scale of the fermions, where all the fermions are in the LLL and hence the only modes entering in the bare coupling are the longitudinal ones.

On the other hand, the  $O(3) \rightarrow O(2)$  symmetry breaking that takes place in the presence of a magnetic field leads to the anisotropic Fierz identities

$$(\gamma_{\parallel}^{\mu})_{il}(\gamma_{\mu}^{\parallel})_{kj} = \frac{1}{2} \left\{ (1)_{il}(1)_{kj} + (i\gamma_5)_{il}(i\gamma_5)_{kj} + \frac{1}{2}(\sigma_{\perp}^{\mu\nu})_{il}(\sigma_{\mu\nu}^{\perp})_{kj} - (\sigma^{03})_{il}(\sigma_{03})_{kj} + \dots \right\}, \quad (2.7)$$

and

$$(\gamma_{\perp}^{\mu})_{il}(\gamma_{\mu}^{\perp})_{kj} = \frac{1}{2} \left\{ (1)_{il}(1)_{kj} + (i\gamma_5)_{il}(i\gamma_5)_{kj} + \frac{1}{2}(\sigma_{\perp}^{\mu\nu})_{il}(\sigma_{\mu\nu}^{\perp})_{kj} - (\sigma^{03})_{il}(\sigma_{03})_{kj} + \dots \right\}, \quad (2.8)$$

where  $\parallel$  and  $\perp$  denotes parallel  $\mu = (0, 3)$  and transverse  $\mu = (1, 2)$  Lorentz indexes with respect to the magnetic field direction. Einstein's summation convention for repeated indices is assumed.

From (2.2),(2.3), and (2.6)-(2.8), one can readily identify the channels considered in  $\mathcal{L}_{int}^{(1)}$  and  $\mathcal{L}_{int}^{(2)}$ . Then, the couplings  $G$  and  $G'$  can be related to  $g_{\parallel}$  and  $g_{\perp}$  through

$$G = \frac{1}{2\Lambda^2}(g_{\parallel}^2 + g_{\perp}^2), \quad G' = \frac{1}{2\Lambda^2}(g_{\parallel}^2 - g_{\perp}^2) \quad (2.9)$$

with  $\Lambda$  the energy scale of the effective theory. At zero magnetic field  $g = g_{\parallel} = g_{\perp}$  and one can use measured physical quantities to find consistent values for  $G$  and  $\Lambda$ . However, at non-zero magnetic field there are no measured parameters that can be used for this purpose. In lieu of arbitrarily assigning values to  $G$ ,  $G'$  and  $\Lambda$ , we can take  $G$  and  $\Lambda$  at their zero-field values, chosen to fix the pion decay constant to  $f_{\pi} = 93$  MeV and the condensate density per quark to  $\langle \bar{u}u \rangle = -(250 \text{ MeV})^3$ , and then assign values to  $G'$  with the constraint  $G' \leq G$ . Notice that  $G' \geq 0$  because when the field increases, so does the occupation of the LLL, hence reinforcing the longitudinal contributions over the transverse ones (see Eq. (2.9)).

The Lagrangian density (2.1) can be also interpreted as an ad-hoc single-flavor effective theory consistent with the symmetries of QCD in a magnetic field. Apart from the subgroup of rotations already mentioned, it is also invariant under baryon symmetry,  $U(1)_B$ , and because of the absence in (2.1) of a fermion mass, chiral symmetry  $U(1)_{\chi}$  is preserved. For other contexts where unconventional four-point interactions in NJL-like models have been considered see [40–43].

## 2.2 Effective Potential in the Mean-Field Approximation

Let us explore now the possibility of the following homogeneous condensates

$$\begin{aligned} \langle \bar{\psi}\psi \rangle &= -\frac{\sigma}{G}, & \langle \bar{\psi}i\gamma^5\psi \rangle &= -\frac{\Pi}{G}, \\ \langle \bar{\psi}i\gamma^1\gamma^2\psi \rangle &= -\frac{\xi}{G'}, & \langle \bar{\psi}i\gamma^0\gamma^3\psi \rangle &= -\frac{\xi'}{G'}, \end{aligned} \quad (2.10)$$

where  $\sigma$ ,  $\Pi$ ,  $\xi$  and  $\xi'$  are constant parameters.

Using them to perform the Hubbard-Stratanovich transformation in the Lagrangian density (2.1), we obtain the partition function in the mean-field approximation

$$\mathcal{Z} = \int \mathcal{D}\bar{\psi} \mathcal{D}\psi \exp [iS(\sigma, \Pi, \xi, \xi')], \quad (2.11)$$

with action

$$\begin{aligned}
S(\sigma, \Pi, \xi, \xi') &= \int d^3x d^4\bar{\psi}(x) (i\gamma^\mu D_\mu - \sigma - i\gamma^5 \Pi - i\gamma^1 \gamma^2 \xi - i\gamma^0 \gamma^3 \xi') \psi(x) \\
&\quad - \frac{V}{2G} (\sigma^2 + \Pi^2) - \frac{V}{2G'} (\xi^2 + \xi'^2).
\end{aligned} \tag{2.12}$$

The corresponding mean-field effective potential is

$$\begin{aligned}
\Omega(\sigma, \Pi, \xi, \xi') &= \frac{\sigma^2 + \Pi^2}{2G} + \frac{\xi^2 + \xi'^2}{2G'} \\
&\quad + \frac{i}{V} \text{Tr} \ln (iD \cdot \gamma - \sigma - i\gamma^5 \Pi - i\gamma^1 \gamma^2 \xi - i\gamma^0 \gamma^3 \xi')
\end{aligned} \tag{2.13}$$

where the trace (Tr) acts in color, Dirac, and coordinate spaces.

At this point, it is convenient to transform to momentum space with the help of the Ritus transformation [44]. This method is based on a Fourier-like transformation that uses eigenfunction matrices  $\mathbb{E}_p(x)$ . The  $\mathbb{E}_p(x)$  are the wave functions of the asymptotic states of charged fermions in a uniform magnetic field. The method yields a fermion Green function that is diagonal in momentum space and explicitly dependent on the Landau levels. Although valid at any field strength, this formalism is particularly convenient to study the strong-field region, where the main contribution comes from the LLL [16, 19, 45].

Using Ritus's approach, the inverse propagator in momentum space [19] takes the form

$$\begin{aligned}
G_l^{-1}(p, p') &= \int d^4x d^4x' \bar{\mathbb{E}}_p^l(x) [iD \cdot \gamma - \sigma - i\gamma^5 \Pi - i\gamma^1 \gamma^2 \xi - i\gamma^0 \gamma^3 \xi'] \delta^{(4)}(x - x') \mathbb{E}_{p'}^l(x') \\
&= (2\pi)^4 \hat{\delta}^{(4)}(p - p') \Theta(l) \tilde{G}_l^{-1}(\bar{p})
\end{aligned} \tag{2.14}$$

with

$$\tilde{G}_l^{-1}(\bar{p}) = [\bar{p} \cdot \gamma - \sigma - i\gamma^5 \Pi - i\gamma^1 \gamma^2 \xi - i\gamma^0 \gamma^3 \xi'], \tag{2.15}$$

and

$$\bar{p}^\mu = (p^0, 0, -\text{Sgn}(qB) \sqrt{2|qB|} l, p^3). \tag{2.16}$$



The  $\mathbb{E}_p^l(x)$ 's are matrix functions given as linear combinations of spin up (+) and down (-) projectors  $\Delta(\pm)$ . For  $q > 0$ , they can be written as

$$\mathbb{E}_p^l(x) = \mathbb{E}_p^+(x)\Delta(+) + \mathbb{E}_p^-(x)\Delta(-), \quad (2.17)$$

with

$$\Delta(\pm) = \frac{I \pm i\gamma^1\gamma^2}{2} \quad (2.18)$$

and

$$\begin{aligned} \mathbb{E}_p^+(x) &= N_l e^{-i(p_0x^0 + p_2x^2 + p_3x^3)} D_l(\rho), \\ \mathbb{E}_p^-(x) &= N_{l-1} e^{-i(p_0x^0 + p_2x^2 + p_3x^3)} D_l(\rho). \end{aligned} \quad (2.19)$$

The index  $l = 0, 1, 2, \dots$  is the Landau level number that characterizes the discretization of the transverse momentum in a magnetic field. Here  $N_l = (4\pi qB)^{1/4}/\sqrt{l!}$  is a normalization constant and  $D_l(\rho)$  denotes the parabolic cylinder function of argument  $\rho = \sqrt{2qB}(x_1 - p_2/qB)$  and index  $l$ .

The coefficient

$$\Theta(l) = \Delta(+)\delta^{l0} + I(1 - \delta^{l0}) \quad (2.20)$$

in (2.14) takes into account the lack of spin degeneracy of the LLL.

To obtain (2.14) we used the orthogonality of the  $\mathbb{E}_p^l$  functions [16]

$$\int d^3x 4\bar{\mathbb{E}}_p^l(x) \mathbb{E}_{p'}^{l'}(x) = (2\pi)^4 \widehat{\delta}^{(4)}(p - p') \Theta(l), \quad (2.21)$$

with  $\bar{\mathbb{E}}_p^l \equiv \gamma^0(\mathbb{E}_p^l)^\dagger\gamma^0$  and  $\widehat{\delta}^{(4)}(p - p') = \delta^{ll'}\delta(p_0 - p'_0)\delta(p_2 - p'_2)\delta(p_3 - p'_3)$ .

After going to Euclidean space, we can use the completeness relation

$$\int \frac{d^4p^E}{(2\pi)^4} \mathbb{E}_p^l(x) \bar{\mathbb{E}}_p^l(x) = (2\pi)^4 \delta^{(4)}(x - x'), \quad (2.22)$$

to invert (2.14) and find

$$G^{-1}(x, x') = \int \frac{d^4p^E}{(2\pi)^4} \frac{d^4p'^E}{(2\pi)^4} \mathbb{E}_p^l(x) G^{-1}(p, p') \bar{\mathbb{E}}_{p'}^{l'}(x'). \quad (2.23)$$

with

$$\oint \frac{d^4 p^E}{(2\pi)^4} \equiv \sum_{l=0}^{\infty} \int \frac{dp_4 dp_2 dp_3}{(2\pi)^4}.$$

With the help of (2.23), the effective potential can be written as

$$\Omega(\sigma, \Pi, \xi, \xi') = \frac{\sigma^2 + \Pi^2}{2G} + \frac{\xi^2 + \xi'^2}{2G'} - N_c q B \operatorname{Tr} \sum_{l=0}^{\infty} \int_{-\infty}^{\infty} \frac{dp_4 dp_3}{(2\pi)^3} \ln \Theta(l) \tilde{G}_l^{-1}(\bar{p}) \quad (2.24)$$

where the integration in  $p_2$  was done using

$$\int_{-\infty}^{\infty} \frac{dp_2}{2\pi} = \int_{-\infty}^{\infty} \frac{dp_2}{2\pi} e^{-i \frac{p_2 p_1}{qB}} \Big|_{p_1=0} = \frac{1}{l_B^2} \delta(p_1) \Big|_{p_1=0} = \frac{1}{l_B^2} \int_{-\infty}^{\infty} dx_1, \quad (2.25)$$

and the trace ( $\operatorname{Tr}$ ) now only acts on the spinorial matrices. Here  $l_B = 1/\sqrt{qB}$  denotes the magnetic length.

Taking into account that the  $l = 0$  term only gets contributions from the subspace of spinors with a single spin projection; spin up (down) for  $q > 0$  ( $q < 0$ ); it can be separated from the rest to write

$$\begin{aligned} \Omega(\sigma, \Pi, \xi, \xi') &= \frac{\sigma^2 + \Pi^2}{2G} + \frac{\xi^2 + \xi'^2}{2G'} \\ &\quad - N_c q B \left[ \int_{-\infty}^{\infty} \frac{dp_4 dp_3}{(2\pi)^3} \ln \left( \det \tilde{G}_0^{-1}(\bar{p}) \right) + \sum_{l=1}^{\infty} \int_{-\infty}^{\infty} \frac{dp_4 dp_3}{(2\pi)^3} \ln \left( \det \tilde{G}_l^{-1}(\bar{p}) \right) \right] \end{aligned} \quad (2.26)$$

Integrating in  $p_4$  we find

$$\begin{aligned} \Omega(\sigma, \Pi, \xi, \xi') &= \frac{\sigma^2 + \Pi^2}{2G} + \frac{\xi^2 + \xi'^2}{2G'} \\ &\quad - \frac{N_c q B}{4\pi^2} \int_{-\infty}^{\infty} |\varepsilon_0| dp_3 - \frac{N_c q B}{4\pi^2} \sum_{\eta=\pm 1} \sum_{l=1}^{\infty} \int_{-\infty}^{\infty} |\varepsilon_{l,\eta}| dp_3, \end{aligned} \quad (2.27)$$

with energy spectrum

$$\begin{aligned} \varepsilon_0^2 &= p_3^2 + (\sigma + \xi)^2 + (\Pi + \xi')^2, \quad l = 0, \\ \varepsilon_{l,\eta}^2 &= p_3^2 + \Pi^2 + \xi'^2 + \sigma^2(1 - X) + 2lqB(1 - X') + \left( \sqrt{\sigma^2 X + 2lqB} + \eta\xi \right)^2, \\ & \quad l \geq 1, \quad \eta = \pm 1 \end{aligned} \quad (2.28)$$

where

$$X = \left(1 + \frac{\Pi \xi'}{\sigma \xi}\right)^2, \quad X' = \left(1 + \frac{\xi'^2}{\xi^2}\right) \quad (2.29)$$

The factor  $qB/4\pi^2$  accounts for the density of states of the Landau levels. The spectrum of the quasiparticles with Landau levels  $l \geq 1$  exhibits a Zeeman splitting ( $\eta = \pm 1$ ) indicating that the new dynamical parameter  $\xi$  enters as an AMM energy term. This is even more evident if we take  $\Pi = \xi' = 0$  in the spectrum, since it becomes equal to the one found in QED with dynamical mass and AMM [19]. No splitting is present in the  $l = 0$  mode, in agreement with the fact that the fermions in the LLL only has one spin projection.

## 2.3 Condensate Solutions

### 2.3.1 Gap Equations

We are interested in the situation where the magnetic field is large enough to have all the quarks lying in the LLL, thus the ground state is dominated by the infrared dynamics and only the first integral in the RHS of (2.27) contributes to the equations. This requires magnetic fields  $qB \sim \Lambda^2 \gtrsim \Lambda_{QCD}^2$ . Such large fields are actually generated in off-central heavy-ion collisions at RHIC.

To determine the dynamical solutions for the four condensates  $\sigma$ ,  $\Pi$ ,  $\xi$  and  $\xi'$ , we need to solve the gap equations

$$\begin{aligned} \frac{\partial \Omega}{\partial \sigma} &= \frac{\sigma}{G} - (\sigma + \xi) \mathcal{I}_0 = 0, \\ \frac{\partial \Omega}{\partial \xi} &= \frac{\xi}{G'} - (\sigma + \xi) \mathcal{I}_0 = 0, \\ \frac{\partial \Omega}{\partial \Pi} &= \frac{\Pi}{G} - (\Pi + \xi') \mathcal{I}_0 = 0, \\ \frac{\partial \Omega}{\partial \xi'} &= \frac{\xi'}{G'} - (\Pi + \xi') \mathcal{I}_0 = 0, \end{aligned} \quad (2.30)$$

where

$$\mathcal{I}_0 = \frac{N_c qB}{2\pi^2} \int_0^\Lambda \frac{dp_3}{\varepsilon_0} \quad (2.31)$$

Here we introduced the momentum cutoff  $\Lambda$  below which the NJL theory is valid. One can check that the solution of (2.30) satisfies

$$\bar{\xi} = \frac{G'}{G}\bar{\sigma}, \quad \bar{\xi}' = \frac{G'}{G}\bar{\Pi} \quad (2.32)$$

Then, the condensates can be found from

$$\int_0^\Lambda \frac{dp_3}{\sqrt{p_3^2 + \left(1 + \frac{G'}{G}\right)^2 (\bar{\sigma}^2 + \bar{\Pi}^2)}} = \frac{2\pi^2}{(G + G')N_c q B} \quad (2.33)$$

Notice that the gap equation (2.33) depends only on the  $U_L(1) \times U_R(1)$ -invariant  $\bar{\sigma}^2 + \bar{\Pi}^2$ , a typical feature of the MC $\chi$ SB phenomenon [13, 38]. Hence, we can, as usual, specialize the condensate configuration with  $\Pi = 0$  and  $\sigma$  constant. As expected for a magnetically catalyzed condensate, no critical coupling is needed for a nontrivial solution to exist.

From (2.32), we see that no solution exists with  $\bar{\sigma} \neq 0$  and  $\bar{\xi} = 0$ , and viceversa. The energetically favored solution has expectation values of both  $\bar{\sigma}$  and  $\bar{\xi}$  different from zero. In the same way that the chiral condensate  $\langle \bar{\psi}\psi \rangle$  gives a dynamical mass to the quasiparticles, the new condensate  $\langle \bar{\psi}i\gamma^1\gamma^2\psi \rangle$  gives them a dynamical AMM.

Once the quarks acquire a dynamical mass, they should also acquire a dynamical AMM. This effect has been found to occur in QED [19] and the appearance of the condensate  $\xi$  in our NJL model is a clear indication that it also occurs in QCD. One can understand the inevitability of a dynamical AMM in the magnetically catalyzed system on the base of symmetry arguments. Once the chiral symmetry is dynamically broken, there is no symmetry protection for the AMM, because it breaks the exact same symmetry. The AMM of the quarks leads to a nonzero dynamical MM for the pair. That the pairs should have a dynamical MM is easy to understand, since they are formed by quarks and antiquarks with opposite spins, so the fermions' AMMs point in the same direction. The magnetic field aligns the pairs's MM leading to a net MM of the ground state.

### 2.3.2 Effect on the Quasiparticle's Effective Mass

The solutions of the gap equations (2.32)-(2.33) are

$$\bar{\sigma} = \left( \frac{2G\Lambda}{G+G'} \right) \exp \left[ -\frac{2\pi^2}{(G+G')N_c q B} \right] \quad (2.34)$$

and

$$\bar{\xi} = \left( \frac{2G'\Lambda}{G+G'} \right) \exp \left[ -\frac{2\pi^2}{(G+G')N_c q B} \right] \quad (2.35)$$

It is important to emphasize that the induced AMM term (2.35) depends nonperturbatively on the coupling constant and the magnetic field. This behavior reflects two important facts: 1) in a massless theory, chiral symmetry can be only broken dynamically, that is, nonperturbatively; and 2) the MC $\chi$ SB phenomenon is essentially a LLL effect. The LLL plays a special role due to the absence of a gap between it and the Dirac sea. The rest of the LLs are separated from the Dirac sea by energy gaps that are multiples of  $\sqrt{2qB}$ , and hence do not significantly participate in the pairing mechanism at the subcritical couplings where the magnetic catalysis phenomenon is relevant. Since the dynamical generation of the AMM is produced mainly by the LLL pairing dynamics, one should not expect to obtain a linear-in-B AMM term, even at weak fields, in sharp contrast with the AMM appearing in theories of massive fermions. In the later case, not only the AMM is obtained perturbatively through radiative corrections, but considering the weak-field approximation means first summing in all the LL's, which contribute on the same footing, and then taking the leading term in an expansion in powers of B [46,47]. Notice that such a linear dependence does not hold, even in the massive case, if the field is strong enough to put all the fermions in the LLL [48].

The effect of the new condensate  $\langle \bar{\psi} i \gamma^1 \gamma^2 \psi \rangle$  is to increase the effective dynamical mass of the quasiparticles in the LLL,

$$M_\xi = \bar{\sigma} + \bar{\xi} = 2\Lambda \exp \left[ -\frac{2\pi^2}{(G+G')N_c q B} \right] \quad (2.36)$$

In QCD, for fields,  $qB \sim \Lambda^2$ , the dimensional reduction of the LLL fermions would constraint the LLL quarks to couple with the gluons only through the longitudinal components. Thus, to consistently work in this regime within the NJL model, we should consider, taking into account (2.9), that  $G' = G$ , so that  $G + G' = 2G$ .

Because the effective coupling enters in the exponential, the modification of the dynamical mass by the magnetic moment condensate can be significant. In consequence, the quasiparticles should be much heavier in our model than in previous studies that ignored the magnetic moment interaction [38]. How much heavier, can be estimated from the logarithm of the ratio between the effective mass (2.36) and the mass found with  $G'$  equal to zero (i.e.  $M_{\xi=0} = 2\Lambda \exp[-2\pi^2/GN_cqB]$ )

$$\ln\left(\frac{M_\xi}{M_{\xi=0}}\right) = \frac{2\pi^2}{GN_cqB} \left(\frac{\eta}{1+\eta}\right) \quad (2.37)$$

Here we used  $G' = \eta G$ , but we know that for  $qB/\Lambda^2 \sim 1$ ,  $\eta \simeq 1$ . Using the values  $G\Lambda^2 = 1.835$ ,  $\Lambda = 602.3$  MeV [49],  $N_c = 3$  and  $q = |e|/3 \simeq 0.1$ , we estimate the RHS of (2.37) as  $(\pi^2/GN_cqB) \simeq 1.8$ . Due to the condensate  $\xi$  the dynamical mass of the quasiparticles increases sixfold. This result shows that at strong fields the new channel of interaction must not be ignored, as it may lead to important physical consequences. One of them is the increase of the critical temperature for the chiral restoration, as we show in the next section.

## 2.4 Critical Temperature

### 2.4.1 Condensate Solutions at Finite Temperature

Our goal now is to calculate the critical temperature for chiral symmetry restoration in the magnetized system. With that aim, we take the LLL approximation in (2.26) and replace the integration in  $p_4$  by the Matsubara's sum

$$\int_{-\Lambda}^{\Lambda} \frac{dp_4}{2\pi} \rightarrow \frac{1}{\beta} \sum_{p_4}, \quad \beta = \frac{1}{T}, \quad p_4 = \frac{(2n+1)\pi}{\beta}, \quad n = 0, \pm 1, \pm 2, \dots \quad (2.38)$$

to obtain

$$\Omega_0^T(\sigma, \Pi, \xi, \xi') = \frac{\sigma^2 + \Pi^2}{2G} + \frac{\xi^2 + \xi'^2}{2G'} - \frac{N_c q B}{\beta} \int_{-\infty}^{\infty} \frac{dp_3}{4\pi^2} \sum_{p_4} \ln [p_4^2 + \varepsilon_0^2] \quad (2.39)$$

Performing the sum in  $p_4$  [50] and introducing the momentum cutoff  $\Lambda$ , we obtain

$$\Omega_0^T(\sigma, \Pi, \xi, \xi') = -N_c q B \int_0^\Lambda \frac{dp_3}{2\pi^2} \left[ \varepsilon_0 + \frac{2}{\beta} \ln(1 + e^{-\beta\varepsilon_0}) \right] + \frac{\sigma^2 + \Pi^2}{2G} + \frac{\xi^2 + \xi'^2}{2G'} \quad (2.40)$$

The gap equations at finite temperature are then given by

$$\begin{aligned} \frac{\partial \Omega_0^T}{\partial \sigma} &= \frac{\sigma}{G} - (\sigma + \xi)[\mathcal{I}_0 + \mathcal{I}_\beta] = 0, \\ \frac{\partial \Omega_0^T}{\partial \xi} &= \frac{\xi}{G'} - (\sigma + \xi)[\mathcal{I}_0 + \mathcal{I}_\beta] = 0, \\ \frac{\partial \Omega_0^T}{\partial \Pi} &= \frac{\Pi}{G} - (\Pi + \xi')[\mathcal{I}_0 + \mathcal{I}_\beta] = 0, \\ \frac{\partial \Omega_0^T}{\partial \xi'} &= \frac{\xi'}{G'} - (\Pi + \xi')[\mathcal{I}_0 + \mathcal{I}_\beta] = 0, \end{aligned} \quad (2.41)$$

where  $\mathcal{I}_0$  is defined in (2.31), and

$$\mathcal{I}_\beta = \frac{N_c q B}{2\pi^2} \int_0^\Lambda \frac{dp_3}{\varepsilon_0} \frac{2e^{-\beta\varepsilon_0/2}}{e^{\beta\varepsilon_0/2} + e^{-\beta\varepsilon_0/2}} \quad (2.42)$$

Once again we can check that the solutions of (2.41) satisfy relations similar to those in Eq. (2.32). Then, the condensates can be found from

$$\int_0^\Lambda \frac{dp_3}{\sqrt{p_3^2 + (1 + \frac{G}{G'})^2 (\bar{\xi}^2 + \bar{\xi}'^2)}} \tanh \left( \frac{\sqrt{p_3^2 + (1 + \frac{G}{G'})^2 (\bar{\xi}^2 + \bar{\xi}'^2)}}{2T} \right) = \frac{2\pi^2}{(G + G')N_c q B} \quad (2.43)$$

Just as in vacuum, the gap equation (2.43) depends only on the  $U_L(1) \times U_R(1)$ -invariant  $\bar{\xi}^2 + \bar{\xi}'^2$ . Hence, we can, as usual, specialize the condensate configuration along the  $\xi$  internal direction and take  $\xi' = 0$ . In Fig. 2.1 we represent the numerical solution of (2.43). Notice that the condensate  $\xi$  decreases continuously with the temperature, vanishing at  $T \sim 0.6M_\xi$ , with  $M_\xi$  the zero- $T$  dynamical mass. This behavior is consistent with that of the order parameter of a second-order phase transition. Equally important, the chiral condensate  $\bar{\sigma}$  evaporates together with  $\bar{\xi}$ , because of the relations (2.32), which, as already pointed out, remain valid at finite temperature.

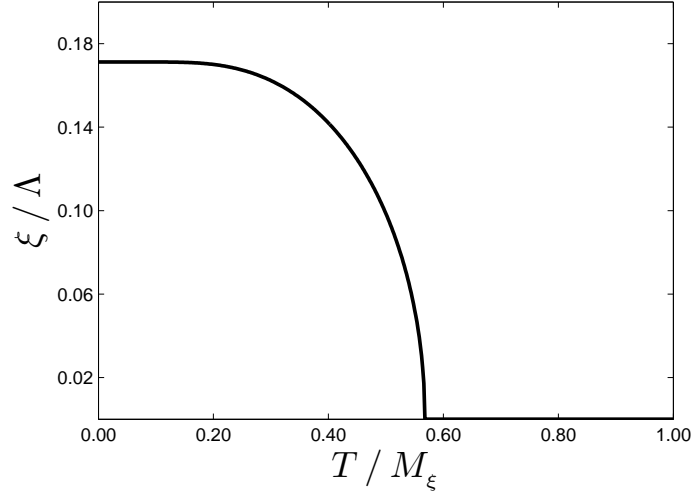


Figure 2.1: Condensate  $\xi$ , normalized by  $\Lambda$ , as a function of the temperature,  $T$ , divided by the zero-temperature dynamical mass  $M_\xi$ .

## 2.4.2 Critical-Temperature Analytical Expression

The critical temperature  $T_{c_x}$  can be analytically found from the condition

$$\left. \frac{\partial^2 \Omega_0^{T_{c_x}}}{\partial \bar{\sigma}^2} \right|_{\bar{\sigma}=\bar{\xi}=0} = \frac{\sigma^2 + \Pi^2}{2G} + \frac{\xi^2 + \xi'^2}{2G'} - \frac{N_c q B}{2\pi^2} \left[ \frac{G + G'}{G} \int_0^\Lambda \frac{dp_3}{p_3} \tanh\left(\frac{\beta_{c_x} p_3}{2}\right) + \frac{2\pi^2}{GN_c q B} \right] = 0 \quad (2.44)$$

We would have arrived at the same condition by taking instead the derivative with respect to  $\bar{\xi}$ . This is a consequence of the proportionality between  $\bar{\sigma}$  and  $\bar{\xi}$ , given in Eq. (2.32), which implies that the two condensates evaporate at the same critical temperature.

Doing the change  $p_3 \rightarrow p_3/T_{c_x}$ , we have

$$\int_0^{\Lambda/T_{c_x}} \frac{dp_3}{p_3} \tanh\left(\frac{p_3}{2}\right) = \frac{2\pi^2}{(G + G')N_c q B}, \quad (2.45)$$

so the resulting critical temperature is

$$T_{c_x} = 1.16\Lambda \exp\left[-\frac{2\pi^2}{(G + G')N_c q B}\right] = 0.58M_\xi \quad (2.46)$$



in agreement with the result found numerically in Fig. 2.1. The fact that the critical temperature is proportional to the dynamical mass at zero temperature, is consistent with the findings in other models [51]. In the present case, since the dynamical mass is increased by the AMM, the critical temperature is proportionally increased.

That the chiral transition is second order can be seen directly from Fig. 2.1, as well as analytically, from the positiveness of the second derivative of  $\Omega$  near the phase transition,

$$\frac{\partial^2 \Omega}{\partial(\bar{\sigma}^2)^2} \Big|_{\beta \approx \beta_C} = \frac{N_c q B \beta_C}{32 \pi^2} \left[ \frac{G + G'}{G} \right]^4 \int_0^{\beta_C \Lambda / 2} dz \frac{\tanh z}{z^3} \left[ 1 - \frac{z}{\sinh z \cosh z} \right] > 0. \quad (2.47)$$

We emphasize that the existence of a unique critical temperature for the evaporation of the two condensates reflects the fact that the condensate  $\xi$  does not break any new symmetry that was not already broken by the condensate  $\sigma$  and the magnetic field, as discussed above.

The simultaneous evaporation of the chiral and magnetic moment condensates has been also reported in the context of lattice QCD [52]. There are, however, important differences in the way the magnetic field influences the system in lattice QCD and in the situation considered in the present work. In Ref. [52] the coupling is supercritical, so the quark have constituent masses even at zero field and the tensor term can be considered to be linear in  $B$ . In our case, however, the quarks acquire their mass and AMM through the MC $\chi$ SB mechanism, so the field-dependence of the condensates is not expandable in powers of  $B$ , and hence can never be linear.

# Chapter 3

## The EoS in the BCS-BEC Crossover of a Simple Fermion System

This Chapter is dedicated to the study of the BCS-BEC crossover for a simple model with multi-fermion interactions. This simple NJL-like model serves as a toy model for a system of quarks with only one flavor and no color degrees of freedoms. The purpose of analyzing this model is to get a qualitative insight on the mechanism driving the BCS-BEC crossover in a relativistic system, and on its implication for the system EoS.

We take into account multi-fermion interactions that account for the attractive interaction between quarks, which gives rise to the diquark formation, the attractive quark-antiquark interaction that gives rise to the chiral condensate, as well as for the repulsive interaction that exists among the diquarks. The inclusion of the multi-fermion interaction with repulsive coupling is inspired by the fact that the same channel that favors diquark formation also gives rise to unfavorable correlations for the cross-channels that would bound quarks from the different diquarks [35]. Without the diquark repulsion, the inclusion of a BEC state in gravitational bound systems, as neutron stars, will become unstable. The results we are reporting in this Chapter are in part contained in the paper [53].

### 3.1 Fermion Model

We use a simple model with fermions having only spin degrees of freedom and exhibiting multiple contact interactions with strengths parameterized by attractive four-fermion couplings  $G_D$  for the fermion-fermion channel,  $G_S$  for the fermion-antifermion one, and by

a repulsive eight-fermion coupling  $\lambda$ .

The corresponding Lagrangian density of our multi-fermion system is given by,

$$\mathcal{L} = \bar{\psi}(i\gamma^\mu\partial_\mu + \gamma_0\mu)\psi + \mathcal{L}_{int} \quad (3.1)$$

where

$$\mathcal{L}_{int} = \frac{G_s}{4}(\bar{\psi}\psi)^2 + \frac{G_D}{4}(\bar{\psi}i\gamma_5 C\bar{\psi}^T)(\psi^T C i\gamma_5\psi) + \lambda [(\bar{\psi}i\gamma_5 C\bar{\psi}^T)(\psi^T C i\gamma_5\psi)]^2 \quad (3.2)$$

In Eq. (3.1), in which we are neglecting the particle current mass,  $\psi$  is a Dirac fermion field,  $C = i\gamma_0\gamma_2$  is the charge conjugation matrix, and  $\mu$  the chemical potential defining the Fermi energy associated in realistic models with the baryon number. The interactions are described by the attractive quark-quark coupling  $G_D$  in the  $J^P = 0^+$  channel which generates the spin-0 diquark condensate, the quark-antiquark coupling  $G_s$ , and the diquark-diquark repulsion  $\lambda$ . The only internal degree of freedom considered in this model is the spin. However, the results we will obtain should not qualitatively change when additional internal fermion degrees of freedom are taken into account. This due to the fact that the essence of the phenomenon under investigation is uniquely related to the change in the nature of the spectrum of the quasiparticles, which is determined by the variation of the diquark-pair binding energy and chemical potential as functions of the strength of the couplings  $G_D$  and  $G_s$ . If  $\lambda = 0$ , the Lagrangian density Eq. (3.1) reduces to that considered in previous works [54, 55]. The interaction term parameterized by  $\lambda$  does not break any symmetry of the original theory. NJL model with eight-fermion contact interaction has also been considered in studying chiral symmetry breaking in Ref. [56].

Now, we bosonize the multi-fermion interactions via Hubbard-Stratonovich transformation. The resulting interaction Lagrangian density is

$$\mathcal{L}_{int} = \frac{1}{2}\chi\Delta\bar{\psi}i\gamma_5 C\bar{\psi}^T + \frac{1}{2}\chi\Delta^*\psi^T C i\gamma_5\psi - \chi'\frac{|\Delta|^2}{G_D} - \frac{m^2}{G_s} \quad (3.3)$$

with gap parameters defined as

$$\Delta = \frac{G_D}{2}\langle\psi^T C\gamma_5\psi\rangle, \quad m = \frac{G_s}{2}\langle\bar{\psi}\psi\rangle, \quad (3.4)$$

and coefficients

$$\chi = 1 + 32\lambda \frac{\Delta^2}{G_D^3}, \quad \chi' = 1 + 48\lambda \frac{\Delta^2}{G_D^3}. \quad (3.5)$$

In the Nambu-Gorkov space,  $\Psi^T = (\psi, \psi_c)$  with  $\psi_c = C\bar{\psi}^T$ , the mean-field propagator is given by

$$G^{-1} = \begin{bmatrix} \gamma^\mu k_\mu + \mu\gamma^0 - m & \chi\Delta^+ \\ \chi\Delta^- & \gamma^\mu k_\mu - \mu\gamma^0 - m \end{bmatrix}. \quad (3.6)$$

with the gap matrices

$$\Delta^+ = \Delta\gamma_5 \quad \Delta^- = \Delta^\dagger\gamma^0\gamma_5\gamma^0 \quad (3.7)$$

The corresponding mean-field partition function

$$\mathcal{Z} = \int \mathcal{D}\bar{\Psi} \mathcal{D}\Psi \exp \left[ i \left( \int \frac{d^4k}{(2\pi)^4} \bar{\Psi} \beta G^{-1} \Psi - \chi' \frac{\Delta^2}{G_D} - \frac{m^2}{G_S} \right) \right] \quad (3.8)$$

is then quadratic in terms of the Nambu-Gorkov fields, and can thus be readily integrated. Going to the finite temperature formalism, the mean-field thermodynamic potential at temperature  $T = 1/\beta$  and chemical potential  $\mu$  takes the form

$$\begin{aligned} \Omega &= -\frac{1}{\beta V} \ln \mathcal{Z} \\ &= -\frac{1}{2\beta} \sum_{n=0}^{\infty} \int \frac{d^3k}{(2\pi)^3} \text{Tr} \ln [\beta G^{-1}(i\omega_n, \mathbf{k})] + \chi' \frac{|\Delta|^2}{G_D} + \frac{m^2}{G_S}, \end{aligned} \quad (3.9)$$

where the Matsubara frequencies of the fermion fields are  $\omega_n = (2n+1)\pi/\beta$ , and  $G^{-1}(i\omega_n, \mathbf{k})$  is the inverse propagator in momentum space.

After Matsubara summation, in the zero-temperature limit we obtain

$$\Omega_0 = - \sum_{e=\pm 1} \int_{\Lambda} \frac{d^3k}{(2\pi)^3} \epsilon_k^e + \chi' \frac{|\Delta|^2}{G_D} + \frac{m^2}{G_S} \quad (3.10)$$

where  $\Lambda$  is an appropriate momentum cutoff to regularize the momentum integral in the ultraviolet, and  $\epsilon_k^e$  the quasiparticle energy spectrum given by

$$\epsilon_k^e = \sqrt{(\epsilon_k - e\mu)^2 + \chi^2 |\Delta|^2}, \quad \epsilon_k = \sqrt{k^2 + m^2}, \quad e = \pm 1. \quad (3.11)$$

The spectra corresponding to different  $e = \pm$  values denote the particle ( $e = +1$ ) and antiparticle ( $e = -1$ ) contributions. Note that the term proportional to  $\lambda|\Delta|^4$  in (3.10) corresponds to a repulsive potential of the bosonized theory [57, 58].

## 3.2 Gap and Mass Equations at Fixed Particle Number Density

The gap equation ( $\partial\Omega_0/\partial|\Delta|$ ) = 0 obtained from (3.10) for  $|\Delta| \neq 0$ , is

$$\int_{\Lambda} \frac{d^3k}{(2\pi)^3} \left( \frac{1}{\epsilon_k^+} + \frac{1}{\epsilon_k^-} \right) = \frac{2(2\chi' - 1)}{G_D(3\chi^2 - 2\chi)} \quad (3.12)$$

The particle mass  $m$  is dynamically determined from the chiral condensate gap equation ( $\partial\Omega_0/\partial m$ ) = 0, which for  $m \neq 0$  is given by

$$\int_{\Lambda} \frac{d^3k}{(2\pi)^3} \frac{1}{2\epsilon_k} \left( \frac{\xi_k^+}{\epsilon_k^+} + \frac{\xi_k^-}{\epsilon_k^-} \right) = \frac{1}{G_S} \quad (3.13)$$

with

$$\xi_k^{\pm} = \epsilon_k \mp \mu \quad (3.14)$$

As usual in the study of the BCS-BEC crossover, we will consider a canonical ensemble where the particle number density,  $n_F = -(\partial\Omega/\partial\mu)$ , is fixed through the Fermi momentum,  $P_F$ , as  $n_F = (P_F^3/3\pi^2)$ . Then

$$\frac{P_F^3}{3\pi^2} = - \int_{\Lambda} \frac{d^3k}{(2\pi)^3} \left( \frac{\xi_k^+}{\epsilon_k^+} - \frac{\xi_k^-}{\epsilon_k^-} \right) \quad (3.15)$$

Solving numerically the system of Eqs. (3.12), (3.13), and (3.15), we can find the gap,  $\Delta$ , chemical potential,  $\mu$ , and dynamical mass,  $m$ , as functions of the couplings  $G_D$ ,  $G_S$  and  $\lambda$ .

## 3.3 Equation of State Along the BCS-BEC Crossover

To consider the possible realization of the BCS-BEC crossover in physical systems, as in the core of neutron stars, it is essential to analyze how the crossover affects the system

EoS. The system's pressure and energy density are determined by the quasiparticles created as perturbation modes over the condensate. It is natural to expect that the nature of the quasiparticles' energy spectra is modified when the system crossovers from BCS to BEC, and that modification has to be reflected in the system EoS.

The energy density and pressure of the system in the zero-temperature limit are respectively calculated from

$$\varepsilon = \Omega_0 + \mu n_F - \Omega_{vac}, \quad p = -\Omega_0 + \Omega_{vac}, \quad (3.16)$$

where we introduced the vacuum contribution  $\Omega_{vac}$  to guarantee that when  $\mu = \Delta = 0$ , the corresponding pressure difference between the system and the outside vacuum becomes zero. In this way, we avoid the introduction by hand, as it was done in Ref. [34], of a bag constant  $B$ , whose value is undetermined for the system under consideration. The vacuum contribution,  $\Omega_{vac}$ , on the contrary, only depends on the chiral condensate that is dynamically determined for this particular model.

The vacuum effective potential is given by

$$\Omega_{vac} = \Omega_0(\mu=0, \Delta=0) = - \int_{\Lambda} \frac{d^3k}{(2\pi)^3} 2\bar{\epsilon}_k + \frac{m_{vac}}{G_S} \quad (3.17)$$

with

$$\bar{\epsilon}_k = \sqrt{k^2 + m_{vac}^2} \quad (3.18)$$

Here, the dynamical mass,  $m_{vac}$ , is obtained from  $(\partial\Omega_{vac}/\partial m_{vac}) = 0$ .

### 3.4 BCS-BEC Crossover and Critical Values

The model contains free parameters that need to be adjusted to solve numerically the system of equations consisting of Eq. (3.12), Eq. (3.13), and Eq. (3.15). We scale all the variables with the cutoff parameter  $\Lambda$ , leaving the Fermi momentum  $P_F$ , the quark-quark coupling  $G_D$ , the quark-antiquark coupling  $G_S$ , and the diquark-diquark repulsion  $\lambda$  as free

parameters to be adjusted to drive the crossover. From now on, the normalized units

$$\begin{aligned}
\tilde{G}_D &\rightarrow G_D \Lambda^2, & \tilde{G}_S &\rightarrow G_S \Lambda^2, & \tilde{\lambda} &\rightarrow \lambda \Lambda^8, \\
\tilde{P}_F &\rightarrow \frac{P_F}{\Lambda}, & \tilde{P} &\rightarrow \frac{P}{\Lambda}, & \tilde{\varepsilon} &\rightarrow \frac{\varepsilon}{\Lambda}, \\
\tilde{\mu} &\rightarrow \frac{\mu}{\Lambda}, & \tilde{\Delta} &\rightarrow \frac{\Delta}{\Lambda}, & \tilde{m} &\rightarrow \frac{m}{\Lambda}, & \tilde{k} &\rightarrow \frac{k}{\Lambda},
\end{aligned} \tag{3.19}$$

are used. Therefore, the cutoff parameter will not explicitly appear in our results. For convenience, we also define

$$\hat{G}_D \rightarrow \frac{\tilde{G}_D}{4\pi^2}, \quad \hat{G}_S \rightarrow \frac{\tilde{G}_S}{4\pi^2}, \quad \hat{\lambda} \rightarrow \frac{\tilde{\lambda}}{4\pi^2}. \tag{3.20}$$

To understand the system dynamics, we analyze the consequence of varying the coupling constants  $\hat{G}_D$ ,  $\hat{G}_S$ , and  $\hat{\lambda}$  for a fixed Fermi momentum,  $\tilde{P}_F = 0.10$ . The results given on Fig. 3.1 and Fig. 3.2 are for a fixed  $\hat{G}_S = 1.20$  while  $\hat{G}_D$  is varying in a convenient interval.

The left panel of Fig. 3.1 shows that the fermion's chemical potential decreases with the increase of the diquark interaction. This behavior is a crucial indication of the crossover. As it is known, the main condition for a relativistic gas to have a bosonic nature is  $\mu < m$  [59]. Then, the  $\hat{G}_D$  value, where  $\mu = m$ , is the critical value for the BCS-BEC crossover. For  $\hat{\lambda} = 0$ , we observe that there exists a coupling critical value,  $\hat{G}_D^{cr} = 0.81$ , beyond which the condition  $\mu < m$  holds. Around the critical value, going from smaller to larger values of the coupling, the crossover from a BCS regime to a BEC one takes place. On the right panel of Fig. 3.1, we see that once the system approaches the BEC regime at  $\lambda = 0$ , the pressure decreases to zero at  $\hat{G}_D^{P_0} = 0.91$ , as it corresponds to a pressureless boson gas. Thus, this is signaling an instability for this strong coupled state of dense matter in gravitational bound systems. Therefore, this behavior would prevent, at  $\lambda = 0$ , the realization of the BCS-BEC crossover in the core of neutron stars. Nevertheless, stars formed by bosons (the so-called boson stars) have been theoretically considered since long ago [60]. In that case the mechanism to stabilize the star against its self-gravity is reached through the contribution to the pressure of self-interacting bosons (i.e. through an interacting potential energy  $U(\Phi) = \lambda\Phi^4$ ) [57].

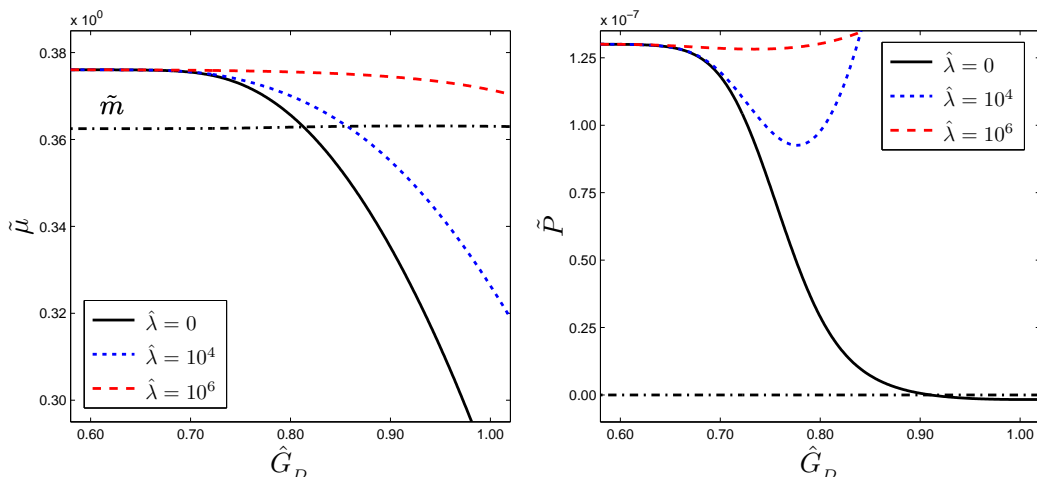


Figure 3.1: Chemical potential  $\tilde{\mu}$  and dynamical mass  $\tilde{m}$  (left panel), and pressure  $\tilde{P}$  (right panel) as a function of the diquark coupling  $\hat{G}_D$  for different values of  $\hat{\lambda}$  at  $\hat{P}_F = 0.10$  and  $\hat{G}_S = 1.20$

Inspired in this idea, in Ref. [34] a term  $\lambda\Delta^4$  was added by hand to model the diquark-diquark repulsion in the thermodynamic potential. With this new term, the pressure increased for  $\hat{G}_D$  values beyond the critical point for the crossover. Similarly, we are working out this same idea, but in a more self-consistent way, starting from a multi-fermion interaction that in the mean-field approximation reproduces the  $\lambda\Delta^4$  potential, and considering a vacuum pressure that is extracted from the same model dynamics. In this approach, we found that while increasing the value of  $\hat{\lambda}$ ,  $\hat{G}_D^{cr}$  increases, but for  $\hat{\lambda} > \hat{\lambda}^{cr} = 11$ , the system pressure never vanishes. It is also apparent that for large values of  $\hat{\lambda}$  (as seen from the left panel of Fig. 3.1),  $\hat{G}_D$  never crosses  $m$  in the considered domain of  $\hat{G}_D$  values. If we continue increasing  $\hat{G}_D$  beyond the domain considered in Fig. 3.1 we find that for values far from the critical point of the BSC-BEC crossover the pressure starts to increase even at  $\hat{\lambda} = 0$ . This is due to the fact that the gap turns out to be so large that its contribution to the quasiparticle spectrum becomes the leading one in the effective potential (4.18), hence leading the pressure behavior.



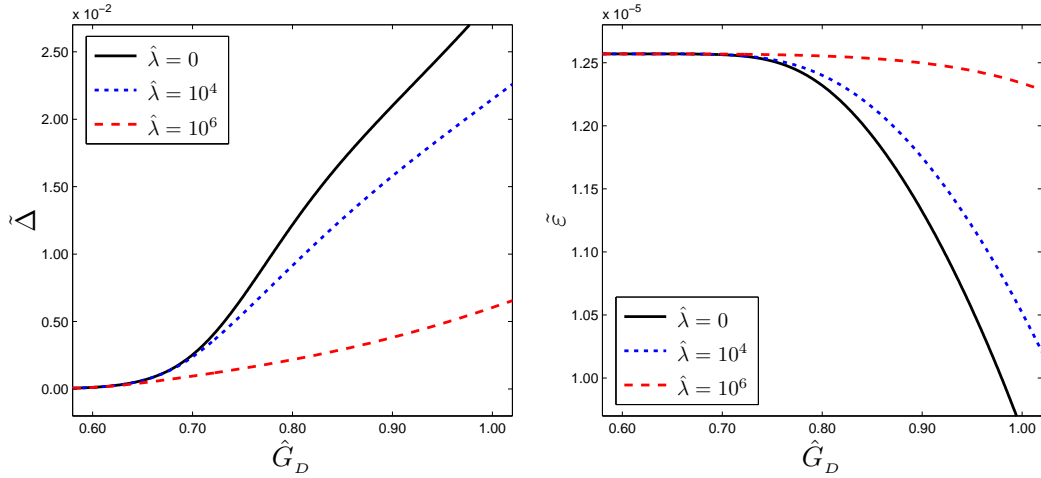


Figure 3.2: Gap parameter  $\tilde{\Delta}$  (left panel), and energy  $\tilde{\varepsilon}$  (right panel) as a function of the diquark coupling  $\hat{G}_D$  for different values of  $\hat{\lambda}$  at  $\tilde{P}_F = 0.10$  and  $\hat{G}_S = 1.20$

In the left panel of Fig. 3.2, we show that the gap parameter starts increasing as the chemical potential begins its decline with increasing  $\hat{G}_D$ . On the other hand, increasing the repulsion between the diquarks ( $\hat{\lambda}$ ) produces a gap decrease while slowing down the decrease of the chemical potential. In the right panel of Fig. 3.2, we show the energy density  $\hat{\varepsilon}$ , which decreases as  $\hat{G}_D$  increases as a consequence of the increase of the diquark gap that makes the condensation energy larger. The repulsion of the diquarks slows down the decline of  $\hat{\varepsilon}$ , since it decreases  $\Delta$ , as it was just discussed.

The diquark-diquark repulsion affects the quasiparticle energy spectrum (see Eq. (3.11)). To check that it is the case, we investigate what is the nature of the quasiparticle spectra for  $\hat{G}_D$  values at both sides of  $\hat{G}_D^{cr}$ . On the left panel in Fig. 3.3, we can see that at  $\hat{\lambda} = 0$  the quasiparticle spectra corresponding to coupling constants smaller and larger than  $\hat{G}_D^{cr}$  correspond to fermion-like and boson-like behaviors, respectively. That is, for  $\hat{G}_D < \hat{G}_D^{cr}$ , the minimum of the dispersion relations occurs at  $\tilde{k} = \sqrt{\tilde{\mu}^2 - \tilde{m}^2}$ , with excitation energy given by the gap  $\Delta$ , a behavior characteristic of quasiparticles in the BCS regime. On the

other hand, for  $\hat{G}_D > \hat{G}_D^{cr}$ , the minimum of the corresponding spectrum occurs at  $\tilde{k} = 0$ , with excitation energy  $\tilde{k} = \sqrt{\tilde{\mu}^2 - \tilde{m}^2 + \Delta^2}$ , which is typical of Bosonic-like quasiparticle. Therefore, it is corroborated that  $\hat{G}_D^{cr}$  is the threshold value for the BCS-BEC crossover in this model. An additional indication of the crossover can be seen from the variation of the gap parameter  $\Delta$  on the right side of Fig. 3.2. As the system crossovers to the BEC regime, the gap becomes significantly larger, thus making the coherence length of the diquark pair  $\xi \sim 1/\Delta$  smaller. On the right panel in Fig. 3.3, we show the spectrum for  $\hat{\lambda} = 10^6$ . It shows that the spectrum have changed and have a fermionic nature for both values of  $\hat{G}_D$  that were previously considerer on the left panel. This is in agreement with the fact that when we increase  $\hat{\lambda}$ , the critical value  $\hat{G}_D^{cr}$  also increases.

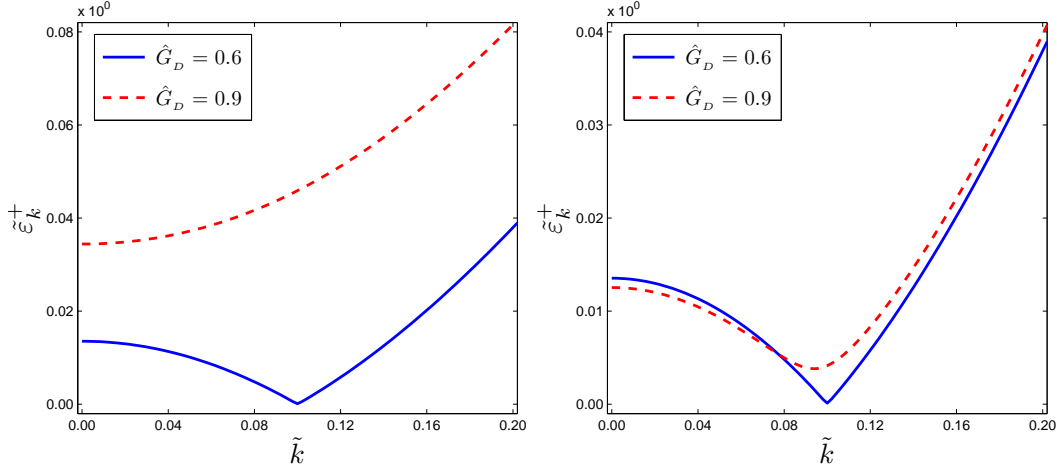


Figure 3.3: Spectrum  $\tilde{\epsilon}_k^+$  as a function of the wave vector  $\tilde{k}$ . On the left panel, we have  $\hat{\lambda} = 0$ , and on the right  $\hat{\lambda} = 10^6$ .

An important goal here is to determine the significance of the diquark-diquark repulsion in the stable realization of the BCS-BEC crossover. We accomplish this by searching for the parameter space where this scenario can be realized at  $\hat{\lambda} = 0$ , and then, with the inclusion of  $\hat{\lambda}$ .

The required condition to have a stable BEC region is that the pressure is kept positive after the crossover. Fig. 3.4 shows the stability windows in the  $\hat{G}_D - \hat{G}_S$  plane. On the left panel, we show the solution for  $\tilde{P}_F = 0.10$ , and on the right panel for  $\tilde{P}_F = 0.20$ . The solid line (blue) marks the crossover condition (points where  $\mu = m$ ). The BEC regime is found to right of this line. The dashed line (black) denotes the zero-pressure condition, which separates a negative pressure regime to the right from a positive pressure one to the left. The short-dashed line (red) separates the massless region (below), characterized by zero chiral condensate, from the massive region (above). The region of parameters where the crossover can occur is given by the intersection of the three lines. Comparing the two graphs we see that the stability region shrinks as  $\tilde{P}_F$  increases, that is, a larger density tends to favor BCS over BEC, as physically expected. For fixed density and  $\hat{G}_D$ , the stability window narrows for larger  $\hat{G}_S$ , indicating that the difference between the system and vacuum pressures becomes smaller with larger chiral coupling. The stability window completely disappears at  $\hat{\lambda} = 0$  when  $\tilde{P}_F = 0.23$ .

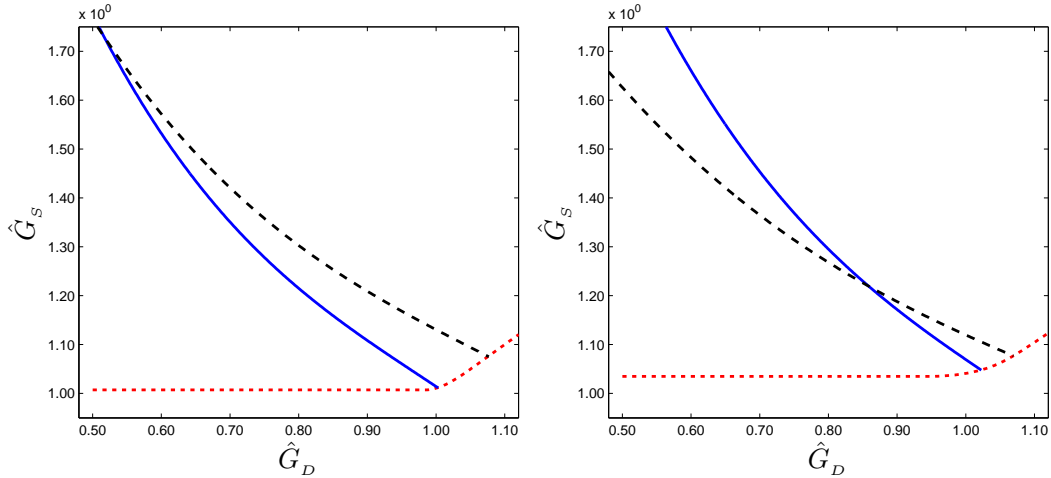


Figure 3.4: Mapping of the region on which the BSC-BEC Crossover take place for  $\hat{\lambda} = 0$ . On the left panel  $\tilde{P}_F = 0.10$ , and on the right panel  $\tilde{P}_F = 0.20$

If we switch to a nonzero  $\lambda$ , the line marking the zero pressure moves up, while the

solid line remains almost at the same place. The stability region has expands in the  $G_D$ - $G_S$  plane. Fig. 3.5 shows the stability windows at  $\hat{\lambda} = 50$  for two different Fermi momenta,  $\tilde{P}_F = 0.10$  (on the left panel) and  $\tilde{P}_F = 0.20$  (on the right panel). The stability window still shrinks with a larger particle density, but it now covers a larger parameter space including higher densities than at  $\hat{\lambda} = 0$ .

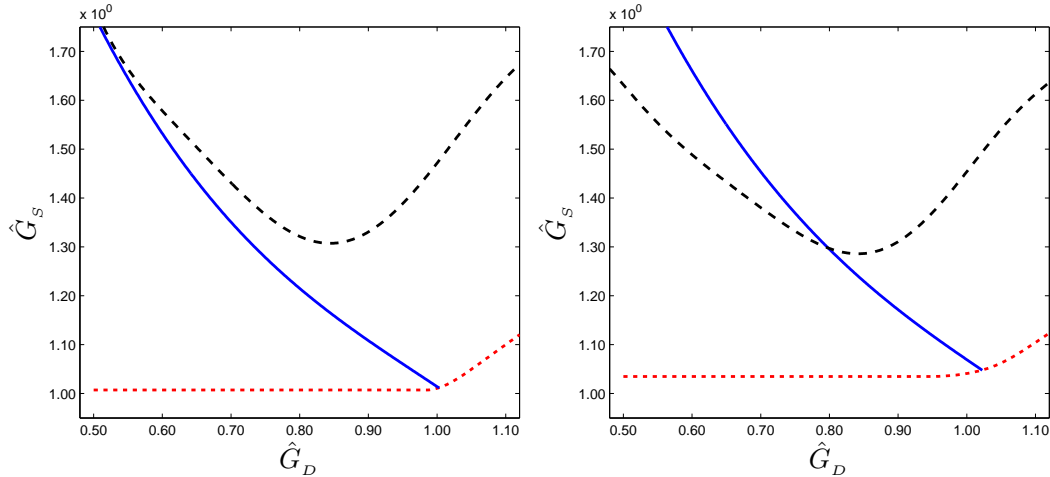


Figure 3.5: Mapping of the region on which the BSC-BEC Crossover take place for  $\hat{\lambda} = 50$ . On the left panel  $\tilde{P}_F = 0.10$ , and on the right panel  $\tilde{P}_F = 0.20$

Then, this result is an indication that it may not be justified to neglect the diquark-diquark repulsion when investing the possible realization of the stable BEC phase. This interesting fact serves as motivation to include the diquark repulsion in a realistic model like the one investigated in the next chapter.

# Chapter 4

## BCS-BEC Crossover for Strongly Coupled 2CS Matter

In this Chapter, we analyze the strongly coupled 2SC phase. The 2SC condensate consists of spin-0 Cooper pairs formed by the  $u$  and  $d$  quarks. The interaction in the QCD one-gluon exchange vertex is attractive in the antitriple channel, which is antisymmetric in flavor, and color.

The purpose of exploring this phase is to relate our research with a realistic model that can be applied to the interiors of compact astrophysical objects like neutron stars. The density in their interior is bounded by hydrostatic equilibrium, augmented to be  $\rho < 10\rho_s$  where  $\rho_s = 10^{14}$  g/cm<sup>3</sup> is the saturation nuclear density. At such densities, the interaction between the quarks is strong. Furthermore, matter in the bulk of compact stars should be neutral with respect to electrical as well as color charges, and remain in  $\beta$ -equilibrium [61]. With that goal in mind, we impose conditions of neutrality and  $\beta$ -equilibrium. These constraints could substantially influence the pairing dynamics between quarks and impose nontrivial relations between the chemical potentials of different quarks. We explore the intermediate density region where chiral symmetry has been broken but we have not reach the confined phase ( $\rho_s < \rho < 5\rho_s$ ). This is the region of the strongly coupled 2SC that, as we mentioned before, is free of the chromomagnetic instabilities. Our expectation is that a smooth BSC-BEC crossover take place by increasing the attractive coupling between the quarks forming the diquarks.

## 4.1 2SC Model

The NJL model with the appropriate pairing channels to describes the 2SC phase is given by the Lagrangian density

$$\begin{aligned} \mathcal{L}_{2SC} = & \bar{\psi}_i^a (i\gamma^\mu \partial_\mu + \gamma^0 \bar{\mu}) \psi_i^a + G_S (\bar{\psi}\psi)^2 + G_D (i\bar{\psi}_C \varepsilon \epsilon^a \gamma_5 \vec{\sigma} \psi) (i\bar{\psi} \varepsilon \epsilon^a \gamma_5 \vec{\sigma} \psi_C) \\ & + \lambda [(i\bar{\psi}_C \varepsilon \epsilon^a \gamma_5 \vec{\sigma} \psi) (i\bar{\psi} \varepsilon \epsilon^a \gamma_5 \vec{\sigma} \psi_C)] , \end{aligned} \quad (4.1)$$

where we are neglecting the current mass of the quarks. Here,  $\psi_C = C\bar{\psi}^T$  is the charge-conjugate spinor,  $C = i\gamma^2\gamma^0$  is the charge conjugation matrix,  $(\varepsilon)^{ik} = \varepsilon^{ik}$  and  $(\epsilon^a)^{bc} = \epsilon^{abc}$  are the antisymmetric tensors in the flavor and in the color spaces, respectively, and  $\bar{\mu}$  is the matrix chemical potential. As in the simple model, we have introduced a diquark-diquark repulsive interaction parameterized by a coupling constant  $\lambda$ .

We can notice that the color structure of the condensate  $(i\bar{\psi}_C \varepsilon \epsilon^a \gamma_5 \vec{\sigma} \psi) \sim \varepsilon_{ik} \epsilon^{abc}$  is anti-symmetric in color as well as in flavor and in Dirac indexes. It has an arbitrary orientation in the color space, and by making use of the global color transformations, the orientation is conveniently fixed in the third blue direction. In this case, the Cooper pairs in the 2SC phase are made of the  $r$  and  $g$  quarks only in a reduced SU(2) flavor symmetry. The unpaired  $b$  quarks give rise to gapless quasiparticles.

We impose  $\beta$ -equilibrium by taking into account a density of electron in order to keep the reactions

$$d \rightarrow u + e^- + \bar{\nu}_e \quad \text{and} \quad u + e^- \rightarrow d_b + \bar{\nu}_e \quad (4.2)$$

at the same rate.

On the other hand, the electric neutrality requires

$$n_d \simeq 2n_u \quad (4.3)$$

where  $n_u$  is the number of u quarks (with electric charge  $+\frac{2}{3}$ ) and  $n_d$  the number of d quarks (with electric charge  $-\frac{1}{3}$ ), even in the presence of a non vanishing electron density. This

condition is implicit in the introduction of the electric chemical potential  $\mu_e$ . Similarly, the color neutrality is implicit in the introduction of the color chemical potential  $\mu_8$ .

The matrix  $\vec{\mu}$  is

$$\mu_{ij,\alpha\beta} = (\mu\delta_{ij} - \mu_e Q_{ij})\delta_{\alpha\beta} + \frac{2}{\sqrt{3}}\mu_8\delta_{ij}(T_8)_{\alpha\beta} \quad (4.4)$$

where  $Q$  and  $T_8$  represent the generators of the electromagnetic and color gauge group. The quark chemical potential explicit expressions are

$$\begin{aligned} \mu_{ur} &= \mu_{ug} = \mu - \frac{2}{3}\mu_e + \frac{1}{3}\mu_8 \\ \mu_{dr} &= \mu_{dg} = \mu + \frac{1}{3}\mu_e + \frac{1}{3}\mu_8 \\ \mu_{ub} &= \mu - \frac{2}{3}\mu_e - \frac{2}{3}\mu_8 \\ \mu_{db} &= \mu + \frac{1}{3}\mu_e - \frac{2}{3}\mu_8 \end{aligned} \quad (4.5)$$

The effective potential in the NJL model in the mean field approximation is obtained using the standard Hubbard-Stratonovich transformation, performing the functional trace in Matsubara frequencies, and obtaining the zero temperature limit,

$$\Omega_0 = -\frac{\mu_e^4}{12\pi^2} - \frac{1}{4\pi^2} \int_0^\Lambda dp p^2 \sum_j g_j |\varepsilon_j| + \chi' \frac{\Delta^2}{4G_D} + \frac{m^2}{4G_S} \quad (4.6)$$

where the sum in Eq. (4.6) run over twelve degrees of freedom associated with the original ones of the six quarks and six antiquarks. In Eq. (4.6), we have introduced a 3-momenta cut off that regularize the integral in the ultraviolet region. The dispersion relations and degeneracies of the quasiparticles are respectively

$$\begin{aligned} \varepsilon_1 &= \epsilon_p \pm \mu_{ub} && \times 1 \\ \varepsilon_2 &= \epsilon_p \pm \mu_{db} && \times 1 \\ \varepsilon_3 &= E_p^\pm \pm \delta\mu && \times 2 \end{aligned} \quad (4.7)$$

Here, the following notations were used

$$\epsilon_p = \sqrt{p^2 + m^2},$$

$$E_p^\pm = \sqrt{(\epsilon_p \pm \bar{\mu})^2 + \chi \Delta^2}, \quad (4.8)$$

$$\bar{\mu} = \frac{\mu_{ur} + \mu_{dg}}{2}, \quad (4.9)$$

$$\delta\mu = \frac{\mu_{dg} - \mu_{ur}}{2}, \quad (4.10)$$

$$\chi' = 1 + \lambda \frac{3 \Delta^2}{4 G_D^3}, \quad \chi = 1 + \lambda \frac{1 \Delta^2}{2 G_D^3} \quad (4.11)$$

Explicitly working out the sum in Eq. (4.6), we rewrite the thermodynamical potential as

$$\begin{aligned} \Omega_0 = & -\frac{\mu_e^4}{12\pi^2} - \frac{2}{\pi^2} \int_0^\Lambda dp p^2 \epsilon_p - \frac{1}{\pi} \int_0^{\sqrt{\mu_{ub}^2 - m^2}} dp p^2 (\mu_{ub} - \epsilon_p) \\ & - \frac{1}{\pi} \int_0^{\sqrt{\mu_{ub}^2 - m^2}} dp p^2 (\mu_{ub} - \epsilon_p) - \frac{2}{\pi^2} \int_0^\Lambda dp p^2 (E_p^+ + E_p^-) \\ & + \chi' \frac{\Delta^2}{4G_D} + \frac{m^2}{4G_S} - \Theta(\delta\mu - \chi^{1/2} \Delta) F \end{aligned} \quad (4.12)$$

The last term in Eq. (4.12) signalizes where the 2SC phase becomes unstable, that is when  $\delta\mu > \chi^{1/2} \Delta$ . The  $F$  function is given by

$$\begin{aligned} F = & \Theta(\delta\mu - \sqrt{(m - \bar{\mu})^2 + \chi \Delta^2}) \left[ \int_0^{P_+} dp p^2 (\delta\mu - E_p^-) + \Theta(\bar{\mu} - m) \int_{P_-}^{P_+} dp p^2 (\delta\mu - E_p^-) \right] \\ & + \Theta(\delta\mu - \sqrt{(m + \bar{\mu})^2 + \chi \Delta^2}) \int_0^{P_-} dp p^2 (\delta\mu - E_p^+) \end{aligned}$$

where

$$\mu_\pm = \bar{\mu} \pm \sqrt{\delta^2 - \chi \Delta^2}, \quad P_\pm = \sqrt{\mu_\pm - m^2}$$

It is important to check that in the BCS-BEC crossover region the condition  $\delta\mu < \chi^{1/2} \Delta$  is satisfied.



## 4.2 Gap Equation and Neutrality Conditions at Fixed Particle Density

The BCS-BEC crossover will be characterized by gap parameter  $\Delta$ , mass  $m$ , and chemical potentials  $\mu$ ,  $\mu_e$ , and  $\mu_8$ , obtained by minimizing the thermodynamic potential with respect to the gap and mass respectively

$$\frac{\partial\Omega}{\partial\Delta} = 0 \quad \frac{\partial\Omega}{\partial m} = 0 \quad (4.13)$$

and by solving the neutrality equations

$$\frac{\partial\Omega}{\partial\mu_e} = 0 \quad \frac{\partial\Omega}{\partial\mu_8} = 0 \quad (4.14)$$

and the density equation

$$n_F = -\frac{\partial\Omega}{\partial\mu} \quad (4.15)$$

The particle number density  $n_F$  is fixed through the Fermi momentum  $n_F = \frac{P_F^3}{3\pi^2}$

The dimensional coupling constant  $G_s$  and the momentum integration cutoff  $\Lambda$  are adjusted to fit the pion decay constant to be  $f_\pi = 93$  MeV, and the condensate density per quark to  $\langle \bar{u}u \rangle = -(250 \text{ MeV})^3$  like in Ref [37, 61]. This fixes the value of  $\Lambda = 653$  MeV, and  $G_s = 2.14\Lambda^2$ . Without loss of generality, we choose  $G_D$  to be proportional to  $G_s$  as follows

$$G_D = \eta G_s \quad (4.16)$$

where  $\eta$  is a dimensionless parameter of order 1. We also introduce the normalized coupling constants

$$\tilde{G}_s \rightarrow \frac{G_s}{\Lambda} \quad \tilde{G}_D \rightarrow \frac{G_D}{\Lambda} \quad \tilde{\lambda} \rightarrow \lambda \Lambda^8$$

In this way, the model parameter setting takes a value of  $\tilde{G}_s = 2.14$  for the chiral condensate coupling. However, this coupling has not been measured in extreme condition

of high densities. Changing the density scale will modify  $\Lambda$  and may also modify the relation between  $\Lambda$  and  $G_s$ . There is no complete certainty that the coupling will remain at the same values. Our study, therefore, will include values of  $\tilde{G}_s$  at and close to 2.14.

### 4.3 Equation of State Along the BCS-BEC Crossover

The system EoS is determined in the same way as in Chapter 3. The energy density and pressure of the system in the zero-temperature limit are respectively calculated from the quantum-statistical average of the energy momentum tensor. They are given by

$$\varepsilon = \Omega_0 + \mu n_F - \Omega_{vac}, \quad p = -\Omega_0 + \Omega_{vac}, \quad (4.17)$$

where we introduced the vacuum contribution  $\Omega_{vac}$  to guarantee that when the gaps and the chemical potentials vanish, the corresponding pressure difference between the system and the outside vacuum becomes zero. The vacuum contribution,  $\Omega_{vac}$  only depends on the chiral condensate that is dynamically determined for this model by

$$\Omega_{vac} = \Omega_0(\mu_{i\alpha}=0, \Delta=0) = -12 \int_{\Lambda} \frac{d^3k}{(2\pi)^3} \bar{\epsilon}_k + \frac{m_{vac}}{4G_s} \quad (4.18)$$

were

$$\bar{\epsilon}_k = \sqrt{k^2 + m_{vac}^2}. \quad (4.19)$$

The dynamical mass in vacuum,  $m_{vac}$ , is obtained from  $(\partial\Omega_{vac}/\partial m_{vac}) = 0$ .

### 4.4 Numerical Results: EoS in the 2SC Phase

The condition that characterizes the BCS-BEC crossover in the simple model of Chapter 3 was that the baryonic chemical potential  $\mu$  crosses the value of the mass  $m$ . However, the 2SC model has condensates that takes place only between an anti-symmetric mixture, in color and flavor, of the  $u$  and  $d$  flavor quarks with  $g$  and  $r$  colors. Then, the BCS-BEC

crossover in the 2SC phase, for only  $g$  and  $r$  color quarks, will take place when the effective chemical potential  $\bar{\mu}$  of the quasiparticles with diquark gaps, defined in Eq. (4.9), crosses the value of the corresponding dynamical mass. On the other hand, since the  $b$  quarks do not participate in the pairing, they always maintain their fermion nature.

We explore first the crossover for a fixed value of  $\tilde{G}_S = 2.14$  at  $\lambda = 0$ . On the right panel of Fig. 4.1, we show the behavior of the vacuum mass  $m_{vac}$  vs  $\tilde{G}_S$ . At  $\tilde{G}_S = 2.14$ , it is obtained  $m_{vac} = 330$  MeV. On the left panel of Fig. 4.1, we show the values of  $\tilde{G}_D^{cr}$  for the BCS-BEC crossover as a function of the baryonic density. Here,  $n_s$  is the ratio between the density and the nuclear saturation density  $\rho_s$  ( $\rho = n_s \rho_s$ ). It is important to notice that the condition  $\eta < 1$  is satisfied at the crossover only for  $n_s < 1$ . Therefore, to have the crossover at densities higher than the nuclear density, the value of  $\eta$  should be greater than 1. We also notice that the crossover disappears for density values for  $n_s > 3.4$ , where only a BCS phase is realized.

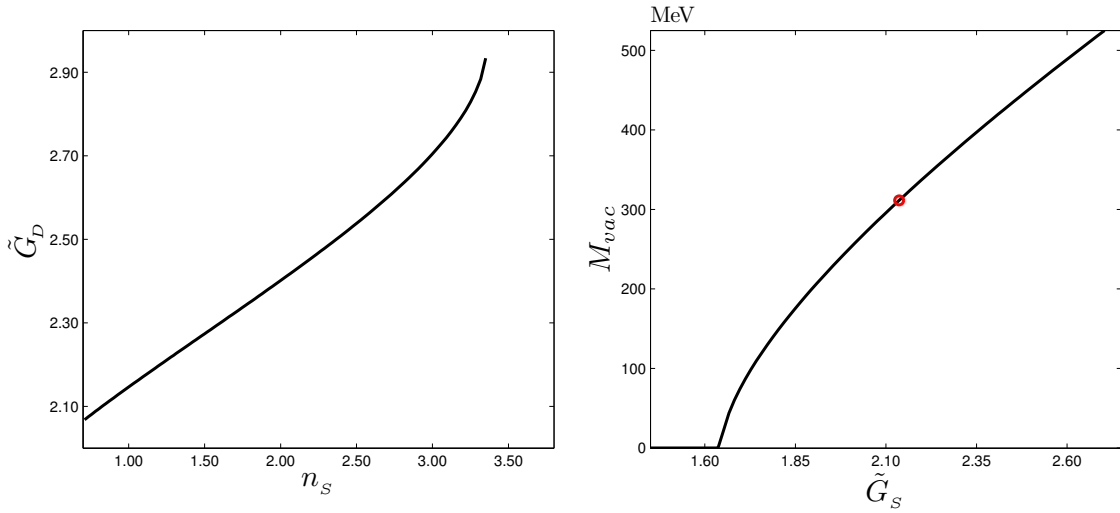


Figure 4.1: Values of the critical coupling  $\tilde{G}_D$  for the crossover at  $\tilde{G}_S = 2.14$  and  $\tilde{\lambda} = 0$  as a function of the baryon density (left pane). Dynamical mass vs  $\tilde{G}_S$  at  $\tilde{\lambda} = 0$  (right panel)

From now on, besides fixing  $\tilde{G}_s = 2.14$ , we also fix the density to  $n_s = 2$  in Figs. 4.2 to 4.5. In Fig. 4.2, we show the behavior for the dynamical mass  $m$ , the effective chemical potential  $\bar{\mu}$ , and the pressure  $P$  for  $\lambda = 0$  and  $\lambda = 200$ . On the left panel, the BSC-BEC crossover take place around  $\eta = 1.10$  for  $\lambda = 0$ . The diquark repulsion moves the crossover to  $\eta = 1.12$ . On the other hand, the corresponding pressures do not decrease in the range of values plotted in the right panel of Fig. 4.2. For lower values of  $\eta$ , the 2SC phase enters the instability region of the g2SC. Then, we conclude that the system is stable for  $\eta > 0.9$  even when it crosses to the BEC region. When  $\lambda$  increases, the pressure increases as expected by the repulsion between diquarks.

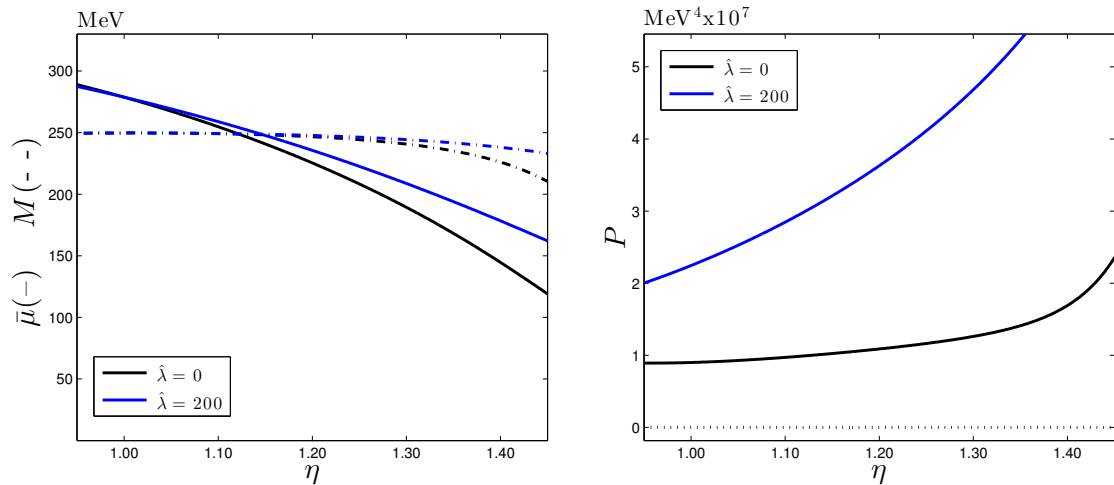


Figure 4.2: Crossover and Pressure at  $\tilde{G}_s = 2.14$  for  $\hat{\lambda} = 0$ (solid line), and  $\hat{\lambda} = 200$ (dotted line)

The behavior of  $\Delta$  is shown on the left panel of Fig. 4.3. Here, like in the simple model, the gap decreases as  $\lambda$  increases. On the right panel, we confirm that the chemical potentials of the  $b$  quarks do not change when the coupling  $\tilde{G}_D$  increases. They remain almost constant until the baryonic chemical potential decreases sufficiently at  $\eta = 1.4$ .

The electric and color chemical potentials are shown on the left and right panel respec-

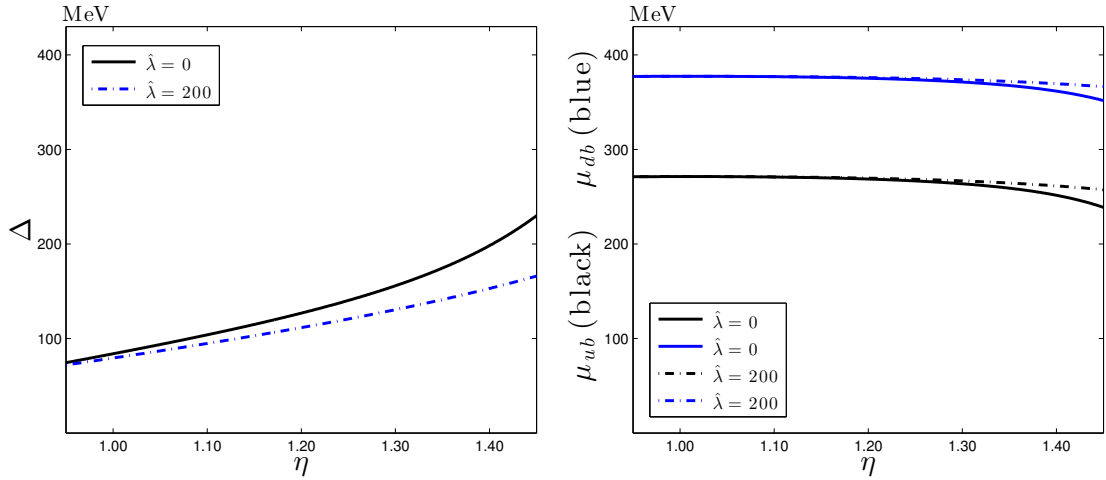


Figure 4.3: Gap  $\Delta$ , and chemical potentials  $\mu_{ub}$  and  $\mu_{db}$  at  $\tilde{G}_s = 2.14$  for  $\hat{\lambda} = 0$ (solid line), and  $\hat{\lambda} = 200$ (dotted line)

tively in Fig. 4.4. The electric chemical potential seems to be fixed by the density  $P_F$  and the  $\hat{G}_s$  coupling. It does not change significantly with  $\hat{G}_D$  and  $\lambda$ . On the other hand, the color chemical potential decreases with  $\hat{G}_D$  at fixed slope, which decreases with  $\lambda$ .

The nature of the quasiparticle spectrum is shown in Fig. 4.5 for the three spectra in Eq. (4.7). In the left panel of Fig. 4.5, the three spectra are plotted vs  $k$  for  $\tilde{G}_D < \tilde{G}_D^{cr}$  (where  $\tilde{G}_D^{cr}$  is the critical value of the coupling in the crossover). Here, each of the quasiparticle spectra has a fermionic nature with a minimum at  $k > 0$ . On the other hand, the spectra of the right panel show the same spectrum after the crossover. The nature of the spectra for the  $b$  quarks remain fermionic, while for the  $r$  and  $g$  quarks, the spectra become bosonic with a minimum at  $k = 0$ . This fact confirms the realization of the BCS-BEC crossover for the quasiparticles formed by combinations of  $r$  and  $g$  quarks.

Finally, on the left panel in Fig. 4.6, we show the realization of the BCS-BEC crossover in the  $\tilde{G}_s - \tilde{G}_D$  plane at different baryonic densities. The blue line shows the crossover at  $n_s = 2$ , which is the same density we considered in Figs. 4.2-4.1. Here, we can follow the

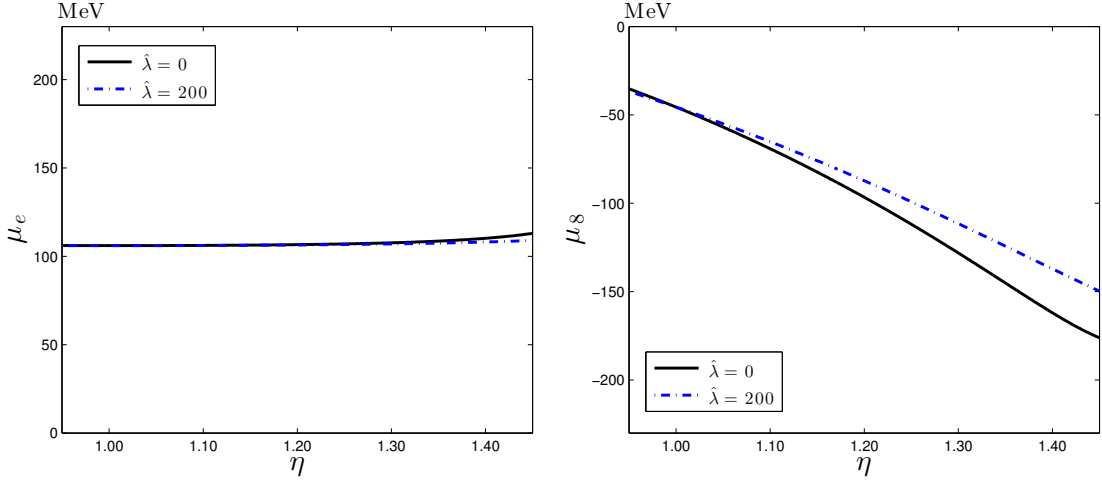


Figure 4.4: Chemical Potentials  $\mu_e$  and  $\mu_8$  at  $\tilde{G}_S = 2.14$

consequences of varying  $\tilde{G}_S^{cr}$  at different densities. The increase of  $\tilde{G}_S^{cr}$  produces a decrease in  $\tilde{G}_D^{cr}$ , and therefore,  $\eta$  becomes smaller. Increasing  $\tilde{G}_S^{cr}$  even more, we reach a point where the pressure becomes negative at the crossover. This point is when the lines pointing at the crossover become wide (upper part in Fig. 4.6). The system is unstable along the crossover for this point and for high enough values of  $\tilde{G}_S^{cr}$ . On the other hand, decreasing the value of  $\tilde{G}_S^{cr}$  increases  $\eta$ . For each density value, the crossover will disappear at a sufficient high value of  $\tilde{G}_D^{cr}$  because the chiral condensate cannot exist for such values of  $\tilde{G}_D^{cr}$  and  $n_s$ .

If we increase the density, the lines characterizing the BCS-BEC crossover move in both positive direction of the plane. At  $n_s = 4$  (green line) the crossover does not occur for  $G_S = 2.14$ . There is a maximum density, shown in Fig. 4.1, at  $n_s = 3.4$ , in which a crossover can take place at  $\tilde{G}_S^{cr} = 2.14$ . The right panel in Fig. 4.6 shows the gaps as function of  $\tilde{G}_D^{cr}$  (remember that  $\tilde{G}_S^{cr}$  decreases as  $\tilde{G}_D^{cr}$  increases, see left panel in Fig. 4.6). The mass  $m$  decreases and the gap  $\Delta$  increases at the crossover with the increase of  $\tilde{G}_D^{cr}$ .

In summary, at strong couplings, a crossover between BCS and BEC regimes can take place. Fig. 4.6 give us a wide view of where the BCS-BEC crossover can take place, and how

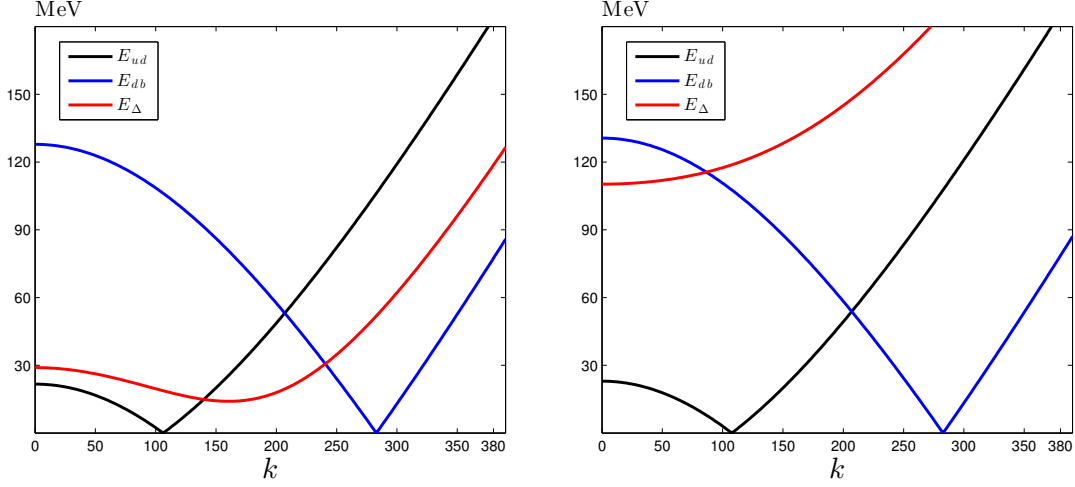


Figure 4.5: Energy Spectrum at  $\eta = 1.0$ (left) and  $\eta = 1.2$ (right)

the crossover moves when changing the couplings or the baryonic density. The pressure never vanishes at the BCS-BEC crossover for values of  $\tilde{G}_S^{cr} \sim 2.14$ . With the results obtained at  $\lambda = 0$ , we can analyze why the pressure never decreases as in the simple model studied in Chapter 3. This apparent contradictory result can be understood by dividing the expression for the pressure in the EoS (Eq. (4.17)), at strong coupling, into two parts

$$P = P_1 + P_2$$

where

$$P_1 = \frac{2}{\pi^2} \int_0^\Lambda dp p^2 (E_p^+ + E_p^-) - \chi' \frac{\Delta^2}{4G_D} - \frac{m^2}{4G_S}$$

$$P_2 = + \frac{\mu_e^4}{12\pi^2} + \frac{2}{\pi^2} \int_0^\Lambda dp p^2 \epsilon_p + \frac{1}{\pi} \int_0^{\sqrt{\mu_{ub}^2 - m^2}} dp p^2 (\mu_{ub} - \epsilon_p) + \frac{1}{\pi} \int_0^{\sqrt{\mu_{db}^2 - m^2}} dp p^2 (\mu_{db} - \epsilon_p).$$

The term  $P_1$  is the contribution to the pressure of the gaped quasiparticles, a term practically equal to the contribution of the gapped quasiparticles in the simple model. The remaining term  $P_2$  is the contribution of the  $b$  quarks and the density of electrons. The neutrality conditions together with  $\beta$ -equilibrium make the chemical potentials  $\mu_{ub}$ ,  $\mu_{db}$ ,

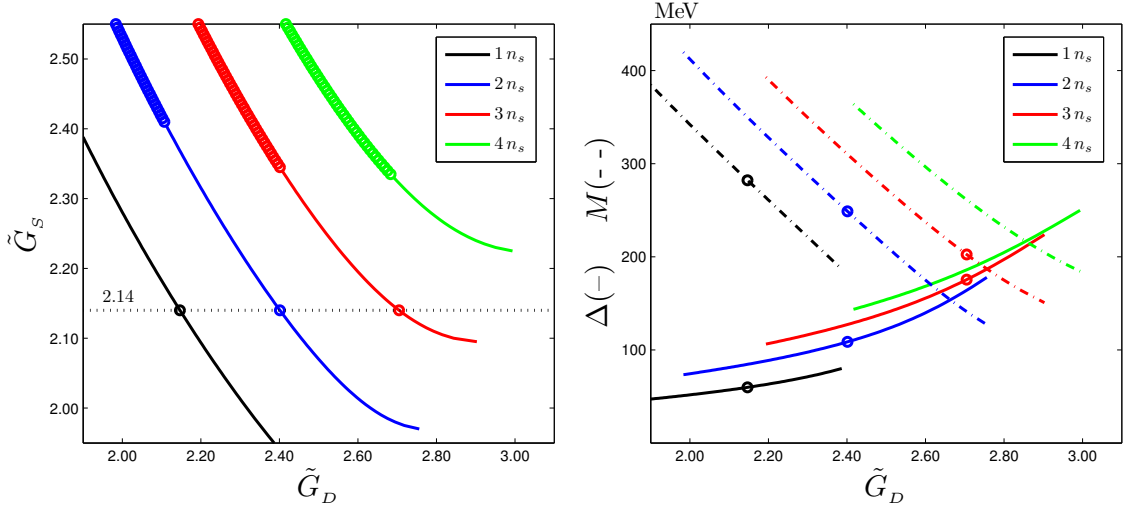


Figure 4.6: Crossover in the  $\tilde{G}_S - \tilde{G}_D$  plane at different  $n_F$

and  $\mu_e$  remains almost constant along the crossover keeping a positive contribution to  $P$ . Hence, the term  $P_2$  is almost constant. On the other hand, the term  $P_1$  does not decrease along the crossover because we are at a strong coupling, and  $P_1$  at this stage had already decreased, as in the simple model. Then, along the crossover,  $P_1$  is a small negative value which remains without significant change for a while, and it increases later (due to the increase in the gap) driving the increase in the  $P$ . As a result, the crossover at  $\tilde{G}_S^{cr} = 2.14$  is stable, and the maximum densities in which the crossover occurs is at  $n_s = 3.4$ . Therefore, it is possible that the BCS-BEC crossover may be realized in the interior of neutron stars and influence their EoS by increasing the system pressure, or modifying the gaps at sufficiently high diquark interaction.



# Chapter 5

## Numerical Method

This section describes the methods employed to numerically solve the equations that were analyzed in this thesis. The analytical procedure of the studied problems begins defining the Lagrangian density and results in the introduction of a grand canonical potential  $\Omega$ . The numerical problem starts there, and could be formulated as follows: we have a thermodynamic potential  $\Omega$  defined as a non-linear integro-differential equation. This thermodynamic potential depends on several fixed parameters (coupling constants, and baryonic density), has to be minimized with respect to the gaps (superconducting and chiral), and has to satisfy neutrality conditions (in the 2SC model) in order to have a stable phase. Once a stable phase is obtained, we can calculate the EoS: pressure and energy density.

A prior analysis of NJL models thermodynamic potentials leads us to conclude the following. The gap equations always have a trivial solution at zero, which is a global minimum if it is a unique solution. Otherwise, the trivial solution is a maximum and a unique positive minimum should be elsewhere, satisfying the density equation. Besides, the neutrality equations have a unique solution once the gaps are fixed. The solutions space is, therefore, limited. Besides, we know certain aspects of the system behavior at the extreme of the explored range, that let us guess the values of the gaps. With this information at hand, we consider that employing a minimization method with equality constraints, like interior point methods or quadratic programming, will be computationally too expensive and not necessary to obtain a satisfactory solution. The problem could be solved efficiently if it is reformulated as a solution of non-linear equations. However, after solving the problem it has to be checked that the gaps effectively minimize the potential.

The objective now is to solve non-linear equations. We start with a function  $\Omega$  that

depends of a set of fixed parameters  $\mathbf{a} = (a_1, a_2, \dots, a_m)^T$ , and unknown variables denoted as  $\mathbf{x} = (x_1, x_2, \dots, x_n)^T$ . We obtain a set of equation partially deriving the function  $\Omega$  with respect to  $n - 1$  of the  $n$  variables (gap parameter, and possible neutrality conditions), and imposing a density equation of the form  $\frac{\partial \Omega}{\partial x_n} + c = 0$ . Then, solving the resulting system of equations, we obtain a stable phase if the gaps minimize  $\Omega$ .

The function  $\Omega$  is proportional the dispersion relation. On the other hand, its partial derivatives are inversely proportional to the dispersion relation, and it is common that the integration in momentum contain a pole. The existence of the pole will spoil the numerical calculations. Therefore, even when a close expressions for the partial derivatives are at hand, the partial derivatives are obtained numerically.

With this goal in main, we divide the computations in three sections

- Numerical integration
- Numerical derivatives
- The solution of a non-linear system of equations

We discuss each one of these points in the remaining part of this chapter. The main objective of the numerical analysis will be to obtain results with enough precision to get a good resolution on the pressure and energy density. This accuracy has to be tested at the end of each calculation since the behavior of our equations are not trivial, and an appropriate bounds could not be made.

## 5.1 Numerical Integration

The numerical integration is the heart in the evaluation of the non-linear equations. This computation is the deepest in the sense that the error introduced here is propagated through the others calculations. Thus, this error has to be strongly bounded with the least computational work possible.

The integrals appearing on the evaluations have the form

$$I = \int_0^\Lambda dk g(k) \quad (5.1)$$

where  $g(k)$  is the dispersion relation of the quasiparticles, and  $\Lambda$  is a positive defined and smooth ultraviolet cutoff parameter, a energy scale limit for our theory that none of our variables could reach. All the variables  $\mathbf{x}$  will be normalized with respect to this parameter.

The integral Eq. (5.1) is discretized using a Gaussian quadrature. In this way, we obtain a better precision with less function evaluation than with the trapezoidal or Simpson methods. The  $n$ -points Gaussian quadrature is given by

$$\int_0^1 dk g(k) = \sum_{i=0}^n A_i g(k_i) \quad (5.2)$$

The nodal points  $x_i$  and the weights  $A_i$  in the Gaussian quadrature are chosen such that the integral Eq. (5.2) is exact for polynomials of degree  $2n + 1$ , as in Ref. [62]. Then, the error term of using approximation Eq. (5.2) is given by

$$E = \frac{g^{(2n)}(\xi)}{(2n)!} \int_0^1 dk \prod_{i=0}^{n-1} (k - k_i)^2 \quad (5.3)$$

where  $g^{(2n)}(\xi)$  is the  $2n$  derivative of  $g$  evaluated at a point  $\xi \in (0, 1)$ .

To have an estimate of the error term using Gaussian quadratures, Table 5.1 shows the integral factor on Eq. (5.3) for different numbers  $n$ .

In principle, a Gaussian quadratures with 10 points will be enough considering that  $g(k)$  is usually smooth. However, we employ a dynamical choice of quadrature for each problem. First, 50 and 40 points are compared. If both results do not coincide at 10 digits of precision, 50 points are used. Otherwise, 40 and 30 points are compared, and we repeat the procedure until we determine the smallest number of points sufficient for the quadrature to be accurate. This dynamical election is done at the first run of the optimization algorithm described on Section 5.3.

Table 5.1: Gaussian Quadrature Error Estimate.

$n$	Error Bound
10	$\frac{g^{2n}(\xi)}{(2n)!} \cdot 1.3950 \times 10^{12}$
20	$\frac{g^{2n}(\xi)}{(2n)!} \cdot 1.2835 \times 10^{-24}$
30	$\frac{g^{2n}(\xi)}{(2n)!} \cdot 1.1720 \times 10^{-36}$
40	$\frac{g^{2n}(\xi)}{(2n)!} \cdot 1.0681 \times 10^{-48}$
50	$\frac{g^{2n}(\xi)}{(2n)!} \cdot 9.7268 \times 10^{-61}$

## 5.2 Numerical Differentiation

As we mentioned before, it is needed to calculate first the Gradient  $\nabla f(\mathbf{x})$ , and then, the second derivatives of a function  $f(\mathbf{x})$ , the Jacobian  $\mathbf{J}f(\mathbf{x})$ . To obtain numerically the gradient and the Jacobian, we use the method of finite difference. This method will be described here for two variables, however, it can be generalized for any number of variables by repeating the steps for each pair of variables. First, we create a mesh of points around the evaluation point  $(x, y)$  as is shown in Fig. 5.1. The space  $h$ , between adjacent points, is a parameter that are adjusted dynamically.

The schemes used to discretized first and second derivatives of  $f$  with respect to a variable  $x$  are

$$\begin{aligned} \frac{\partial f(x, y)}{\partial x} &\approx f_x = \frac{f(x + h, y) - f(x - h, y)}{2h} \\ \frac{\partial^2 f(x, y)}{\partial x^2} &\approx f_{xx} = \frac{f(x + h, y) - 2f(x, y) + f(x - h, y)}{h^2} \end{aligned} \quad (5.4)$$

and similar expressions are obtained for the derivatives with respect to  $y$ . The mixed

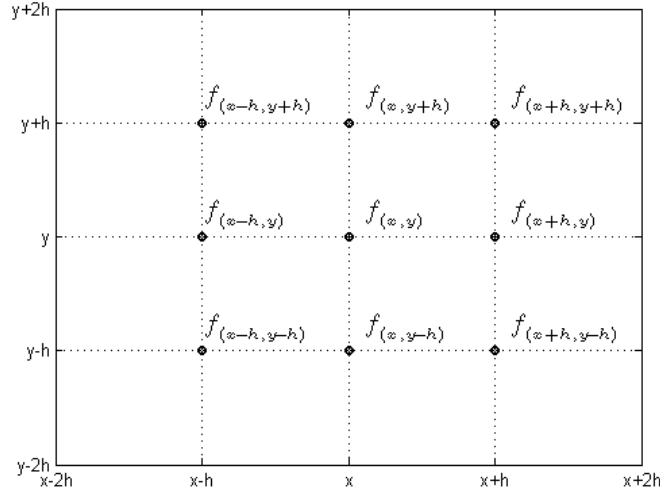


Figure 5.1: Discretization

derivatives that appears on the Jacobian are discretized applying scheme in Eq. (5.4) twice

$$\frac{\partial^2 f(x, y)}{\partial x \partial y} \approx f_{xy} = \frac{1}{2h} \left( \frac{f(x+h, y+h) - f(x-h, y+h)}{2h} - \frac{f(x+h, y-h) - f(x-h, y-h)}{2h} \right) \quad (5.5)$$

$$\frac{\partial^2 f(x, y)}{\partial y \partial x} \approx f_{yx} = \frac{1}{2h} \left( \frac{f(x+h, y+h) - f(x+h, y-h)}{2h} - \frac{f(x-h, y+h) - f(x-h, y-h)}{2h} \right) \quad (5.6)$$

Using Taylor expansion, it can be shown that the error bound on each finite difference evaluation is  $Err = \mathcal{O}(h^2)$ . The parameter  $h$  is usually chosen as  $h = \sqrt{\varepsilon}$ , where  $\varepsilon$  is the machine precision. However, since the explicit expressions for the first derivatives are already known, they are used to chose the appropriate value of  $h$  dynamically. The initial value is  $h = 10^{-8}$ , then, both analytical and numerical first derivatives are compare in order to adjust the value of  $h$ . If  $h = 10^{-8}$  is introducing roundoff errors,  $h$  will be decreased by a factor of 10.

Then, the gradient of  $f(x, y)$

$$\nabla f(x, y) = \begin{pmatrix} \frac{\partial f(x, y)}{\partial x} \\ \frac{\partial f(x, y)}{\partial y} \end{pmatrix} \quad (5.7)$$

is discretized using the grid as in Eq. (5.4), Eq. (5.5) and Eq. (5.6)

$$\nabla f(x, y) \approx \begin{pmatrix} f_x \\ f_y \end{pmatrix} \quad (5.8)$$

The Jacobian of  $f(x, y)$

$$\mathbf{J}f(x, y) = \begin{pmatrix} \frac{\partial^2 f(x, y)}{\partial x^2} & \frac{\partial^2 f(x, y)}{\partial x \partial y} \\ \frac{\partial^2 f(x, y)}{\partial y \partial x} & \frac{\partial^2 f(x, y)}{\partial y^2} \end{pmatrix} \quad (5.9)$$

is discretized as

$$\mathbf{J}f(x, y) = \begin{pmatrix} f_{xx} & f_{xy} \\ f_{yx} & f_{yy} \end{pmatrix} \quad (5.10)$$

Notice that the Function, Gradient, and Jacobian at pint  $(x, y)$  are evaluated using just the 9 points shown in the mesh of Fig. 5.1.

## 5.3 Minimization Method

The problem described at the beginning of the chapter is strictly formulated as a minimization problem with a constraint

$$\min_{x_1, \dots, x_{n-1}} \Omega(\mathbf{x}) \quad \text{subject to} \quad \frac{\partial \Omega}{\partial x_n} + c = 0 \quad (5.11)$$

There are different methods to approach Eq. (5.11): sequential quadratic programming, interior point methods, quadratic penalty methods, etc. However, the number of variables  $n$  in our case is small, from two to four, and the function evaluation is not too expensive; hence, we can reformulate problem Eq. (5.11) in a some what more efficient way that will save some complication inherent in the minimization problem.

The problem, in Eq. (5.11), could be redefined as

$$\mathbf{r}(\mathbf{x}) = 0 \quad \text{subject to} \quad \mathcal{C} > 0 \quad \text{and} \quad |\mathbf{x}^*|_\infty < 1 \quad (5.12)$$

where  $\mathbf{r}(\mathbf{x})$  is the residual function

$$\mathbf{r}(\mathbf{x}) = \begin{pmatrix} r_1(\mathbf{x}) \\ r_2(\mathbf{x}) \\ \dots \\ r_2(\mathbf{x}) \end{pmatrix} \quad (5.13)$$

whit  $r_1(\mathbf{x}) = \frac{\partial \Omega}{\partial x_1}$ ,  $r_2(\mathbf{x}) = \frac{\partial \Omega}{\partial x_2}$ ,  $\dots$ ,  $r_{n-1}(\mathbf{x}) = \frac{\partial \Omega}{\partial x_{n-1}}$ , and  $r_n(\mathbf{x}) = \frac{\partial \Omega}{\partial x_n} + c$ . The last equation represents the density condition, and  $\mathcal{C}$  is the curvature of  $\Omega$  with respect to the variables  $x_1, x_2, \dots, x_{n-1}$ . In other words, the solution  $\mathbf{x}^*$  of Eq. (5.12) also has to be a minimum of  $\Omega$ , but not any minimum, it has to be a global minimum where  $|\mathbf{x}^*|_\infty < 1$ . The last restriction is imposed because of the physics that is being studied. All the variables are normalized with respect to a momentum cutoff  $\Lambda$ . This value is our energy scale and no observable could be even close to its value.

To solve Eq. (5.12), a Newton-like method with a merit function approach is used. Taking into account the characteristics of the method needed, the name of the method is *a merit function approach to solve non-linear equations using a globalized Newton-like method with a Line Search and curvature constrain*. The name of the method summaries the algorithms it uses (for more information about the different parts of the algorithm see [63]).

### 5.3.1 Merit Function

The merit function is designed to measure the progress made by each Newton step. In our case the function is proportional to the residual function  $\mathbf{r}(\mathbf{x})$

$$f(\mathbf{x}) = \frac{1}{2} |\mathbf{r}(\mathbf{x})|^2 \quad (5.14)$$

Equation Eq. (5.14) is the same merit function minimized in the Least Square Problem. However, in this case, the number of equations is equal to the number of variables; then, the minimum  $\mathbf{x}^*$ , if it exists, it will make  $f(\mathbf{x}^*) = 0$ .

### 5.3.2 Newton's Method

Newton's method is an iterative method, which forms a linear model  $M_k(\mathbf{p}_k)$  of the function  $f(\mathbf{p}_k)$  at each iteration  $k$ . The linear model is obtained from the first two terms of the Taylor polynomial of the residual function  $r(\mathbf{x})$ . The root of the model  $M_k(\mathbf{p}_k) = 0$ , gives the step  $\mathbf{p}_k$  to the next approximation

$$\mathbf{x}_{k+1} = \mathbf{x}_k + \mathbf{p}_k \tag{5.15}$$

The model is

$$M_k(\mathbf{p}_k) \equiv r_k + \mathbf{J}_k \mathbf{p}_k \tag{5.16}$$

where  $r_k$  is a short notation for  $r(\mathbf{x}_k)$ ,  $\mathbf{J}_k$  is the Jacobian of  $r_k$  and  $\mathbf{p}_k$  is the Newton's step

$$\mathbf{p}_k = -\mathbf{J}_k^{-1} r_k \tag{5.17}$$

---

#### Algorithm 1 Newton-Method Root Finder

---

**Require:**  $\mathbf{x}_0$  and  $Tol$

**repeat**

    Obtain Newton Step

$$\mathbf{p}_k = -\mathbf{J}_k^{-1} r_k$$

    Update Solution

$$\mathbf{x}_{k+1} = \mathbf{x}_k + \mathbf{p}_k$$

**until**  $f(\mathbf{x}_{k+1}) < Tol$

---

If the first approximation  $\mathbf{x}_0$  is close to the solution  $\mathbf{x}^*$ , Newton method is guaranteed to converge q-quadratically. Its convergence is its main advantage when the approximation is close to the solution.



After a Newton iteration, if the new approximation  $\mathbf{x}_{k+1}$  is close enough to the solution of Eq. (5.14), the method has succeeded; otherwise, the procedure is repeated. To measure how close the approximation  $\mathbf{x}_{k+1}$  is to the solution, the variable  $Tol$  is introduced. Then, the criteria to stop the method is  $f(\mathbf{x}_{k+1}) < Tol$ . The variable  $Tol$  is chosen dynamically. The initial value is  $Tol = 10^{-8}$ , and will be adjusted, by a factor of 10, if needed, i.e. if at the end of the algorithm the four digits of precision are not met.

### 5.3.3 Line Search

The Newton direction,  $\mathbf{p}_k$ , is designed to be a descendent direction

$$\mathbf{p}_k^T \nabla f_k = -\mathbf{p}_k^T \mathbf{J}_k^T \mathbf{r}_k = -|\mathbf{r}_k|^2 < 0 \quad (5.18)$$

if a sufficient small step is taken, it will decrease the merit function and a progress to the solution is guaranteed. However, if big quantities of small steps are taken, the q-quadratic convergency of a full Newton step is lost. There are two common strategies to approach this problem a backtracking line search and a trust region method. Both strategies have similar efficiency, and globalize the Newton method ensuring a progress to the solution at each step. Thus, the strategy used is the line search because it is simpler.

---

#### Algorithm 2 Line Search

---

**Require:**  $\mathbf{p}_k, J_{max}$

Set  $\alpha = 1$

**for**  $J = 0, 1, \dots, J_{max}$  **do**

**if**  $f(\mathbf{x}_k + \alpha_k \mathbf{p}_k) > f(\mathbf{x}_k) + c \alpha_k \nabla f(\mathbf{x}_k)$  **then**

**return**  $\alpha$

**end if**

$\alpha = \frac{1}{2} \alpha$

**end for**

**return**  $\alpha$

---

The line search needs a condition to know if the considered step is accepted or not. The requirement imposed is that the step reduces the merit function Eq. (5.14) in proportion to the step length  $\alpha$  and the  $\nabla f$ .

$$f(\mathbf{x}_k + \alpha_k \mathbf{p}_k) > f(\mathbf{x}_k) + c \alpha_k \nabla f(\mathbf{x}_k) \quad (5.19)$$

Notice that close to the solution,  $\nabla f \simeq 0$ . The parameter  $c$  should be small; we use  $c = 10^4$  which has been used with very good results [64].

The line search strategy is then to modify Newton step as

$$\mathbf{x}_k + \alpha_k \mathbf{p}_k \quad (5.20)$$

first, the full Newton step is tested with  $\alpha_k = 1$ , if it does not satisfy Eq. (5.19) the step is decreased by a factor  $\frac{1}{2}$  and tested again, until a proper step is found or a maximum number of iterations  $J_{max}$  has been reached. Restricting the number of iterations prevents to get stuck accepting small steps, but could let to an increase of the merit function. This is a risk that has to be taken.

### 5.3.4 Global Strategy

There are several points that have to be taken into account in the development of a general strategy. In the search for a global minimum, a common strategy is to create a discrete mesh of points and use the value of each point as initial approximation in Newton method. The solution is expected to satisfy  $|\mathbf{x}|_{\text{inf}} < 1$  due to physical restriction. Besides, in this region, our function has probably just one minimum. Then, we create a mesh, with no more than three or four points per dimension, inside the unit square like is shown in Fig. 5.2.

Each point in the mesh is used as a starting point  $\mathbf{x}_0$  in Newton method and will converge to its own local minimum. When the method finish exploring each initial point, the solutions found are compared. The one that minimizes the potential  $\Omega$  and satisfies the restriction on Eq. (5.12) is chosen. Finally, all the parameters of interest like pressure and

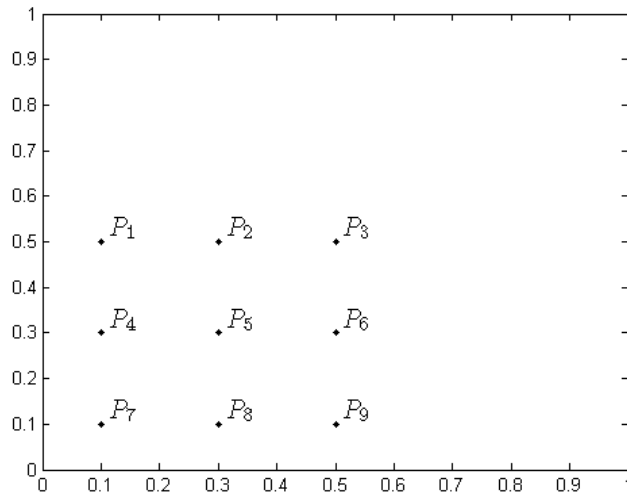


Figure 5.2: Mesh of Initial Points

energy density are calculated, and the accuracy of the results are checked. It is expected that when we change the variables by a value proportional to  $\sim 10^{-5}$ , the parameters of interest do not change by more than a quantity  $\sim 10^{-5}$ . If the parameter changes more than that, the precision is adjusted, and the calculation continues.

The pseudo-code for the complete method is shown below. It does a very good job on all the cases studied on the last chapters, and in reproducing some other result already published [6, 34, 61, 65] similar to the ones handled in this thesis.

---

**Algorithm 3** Newton-Method Root Finder

---

**Require:**  $Mesh = \{M_1, M_2, \dots, M_N\}, IT_{max}$

Begin Local Search

**for**  $k = 1, k \leq N, k \rightarrow k + 1$  **do**

$\mathbf{x}_0 = M_k$

Begin Newton Iteration

**for**  $IT = 0, IT < IT_{max}, IT \rightarrow IT + 1$  **do**

Obtain Newton Step  $\mathbf{p}_k = -\mathbf{J}_k^{-1} \mathbf{r}_k$

Run Line search Algorithm

Update Solution  $\mathbf{x}_{k+1} = \mathbf{x}_k + \mathbf{p}_k$

Check toping Criteria  $f(\mathbf{x}_{k+1}) < Tol$

**end for**

**if**  $IT < IT_{max}$  and  $|\mathbf{x}|_{inf} < 1$  and  $\mathcal{C} > 0$  **then**

Solution Found.....!!!  $SOL(k) = \mathbf{x}_{k+1}$

**else**

Solution not Found...!!!  $SOL(k) = -1$

**end if**

**end for**

Find global Solution

**return** Global Solution

---

# Chapter 6

## Remarks

### 6.1 AMM in Massless Quarks

The first part of this thesis explored chiral symmetry breaking in a magnetic field. In Chapter 2, we used a QCD-inspired theory described by a one-flavor NJL model of interacting massless quarks. The model includes a tensor channel that opened up via the Fierz identities derived from one-gluon exchange interactions in a system where the rotational symmetry has been broken by an external magnetic field.

Within this model, we showed that the  $MC\chi SB$  generates two independent, spin-0 and spin-1, condensates that cannot exist separated one of each other. The spin-0 is the conventional chiral condensate that generates a dynamical mass for the fermions. Here, the pairs are formed by a particle and an antiparticle with opposite spins and charges, and they have their magnetic moments pointing in the same direction. Under an applied magnetic field, the magnetic moments of the pairs orient in the field direction giving rise to an overall magnetic moments of the ground state that is equivalent to a nonzero expectation value of  $\langle \bar{\psi} \Sigma^3 \psi \rangle$ . The new condensate dresses the quasiparticles with a dynamical AMM, as reflected in the way the AMM parameter  $\xi$  enters in the energy spectra. The dynamical AMM produces a Zeeman effect in all the quasiparticles with nonzero Landau levels. For the LLL quasiparticles, there is no Zeeman splitting because only one spin contributes. However, the effect of the AMM in this case is to significantly increase the effective dynamical mass of the LLL quarks, and consequently the critical temperature of the chiral phase transition. As the quasiparticles will be heavier at large fields, compared to their mass when the spin condensate can be ignored, and since they are charged, the electrical conductivity in this

case should be much smaller at strong fields. This will affect the transport properties of this magnetized medium, a topic worth of more investigation for its potential implications for astrophysics.

Previous works on magnetic catalysis of chiral symmetry breaking using analytical approaches [38] have found that the dynamical induced mass increases with the field. Then, it has been a common believe that in the NJL approach the critical temperature of the chiral phase transition increases with the field. However, QCD-lattice calculation has shown the opposite, the critical temperature decreases with the magnetic field. Then, it is an open question, which is attracting much attention, to reconcile those two approaches

## 6.2 BCS-BEC Crossover

The second part of this thesis explored the possibility of a BCS-BEC Crossover in quark matter. In Chapter 3, we started by considering a simple quark system described by a NJL model with one flavor multi-fermion interaction. The model considers attractive channels for particle-antiparticle ( $G_s$ ), particle-particle ( $G_D$ ), and a repulsive diquark-diquark ( $\lambda$ ) channel. For this system, we mapped the coupling  $G_s - G_D$  plane at  $\lambda = 0$  and found out that for a fixed density, where  $P_F < 0.23$ , there exist a closed area of parameter values where the BCS-BEC crossover with positive pressure can take place. We found that, as the strength of the attractive coupling between quarks increases, the chemical potential turns from being larger than the quark mass to being smaller, an indication of the BCS-BEC crossover. This transition was confirmed in the characteristics of its quasiparticle spectrum. For densities bigger than  $P_F < 0.23$ , the pressure decreases to zero before reaching the BCS-BEC crossover. Then, we considered the introduction of a repulsive force between diquarks. The diquarks' repulsion opens and widens the stability windows in the  $G_s - G_D$  plane, where a stable BCS-BEC crossover can occurs for a larger range of densities. It turns out that the diquark-diquark repulsion may affect considerably the stability of the system by increasing its pressure or by changing the spectrum nature.

The qualitative results obtained in Chapter 3 serve as a preliminary step to explore a more realistic model of dense quark matter applicable to the EoS in neutrons stars in Chapter 4. There, we studied a NJL model that describes the pairing channels in the 2SC phase at strong coupling. We explored the range of densities that may be available in compact stars, and imposed neutrality of electric and color charge, as well as,  $\beta$ -equilibrium. Besides, we set  $\hat{G}_s = 2.14$  and  $\Lambda = 653$  MeV to reproduce observable values that agrees with this model at low densities. In this model, we found that a BCS-BEC crossover, with positive pressure, occurs for densities until  $3.4\rho_s$ . Rising the density, the chiral condensate evaporates and the crossover disappears. On the other hand, contrary to the simple model, the pressure never vanished due to the strong coupling on the considered range, the density of electrons, and the unpaired  $b$  quarks, whose nature does not change along the BCS-BEC crossover. Later, we increased the value of  $\hat{G}_s$  and found that the BCS-BEC crossover takes place at smaller values of  $\hat{G}_D$ . For a sufficient high  $\hat{G}_s$ , there is a critical value where the pressure becomes zero. Then, we showed that the introduction of the diquarks repulsion increases the possibility of having higher values for  $\hat{G}_s$ , and what is most important for application to compact stars, it allows to have a stable BCS-BEC crossover at higher densities than  $3.4\rho_s$ .

The results we are reporting in both studies show the importance of the diquark-diquark repulsion. By increasing the repulsion, the parameter window, where the system is stable, increases. Hence, it opens the possibility of having a stable BCS-BEC crossover.

# References

- [1] S. Weinberg, *The quantum theory of fields. vol. 1-3*. Cambridge, UK: Univ. Pr.(1996).
- [2] L. Ginzburg, L. D. Landau, *Zh. Exsp. teor. Fiz.* **20**, 1064 (1950).
- [3] D. J. Gross and F. Wilczek, *Phys. Rev. Lett.* **30**, 1343 (1973); H. D. Politzer, *Phys. Rev. Lett.* **30**, 1346 (1973); S. Coleman and D. J. Gross, *Phys. Rev. Lett.* **31**, 851 (1973).
- [4] S. Hands, *Contemporary Physics* **42**, 4 (2001).
- [5] F. Karsch, *Nucl. Phys.* **A698**, 199 (2002); E. Laermann, *Nucl. Phys. Proc. Suppl.* **63**, 114 (1998); A. Ukawa, *Nucl. Phys. Proc. Suppl.* **53**, 106 (1997).
- [6] M. Alford, C. Kouvaris, and K. Rajagopal, *Phys. Rev. Lett.* **92**, 222001 (2004); *Phys. Rev. D* **71**, 054009 (2005).
- [7] K. Rajagopal, *Nucl. Phys.* **A661**, 150 (1999).
- [8] D. E. Kharzeev, L. D. McLerran, and H. J. Warringa, *Nucl. Phys.* **A803**, 227 (2008).
- [9] V. Skokov, A. Y. Illarionov, and V. Toneev, *Int. J. Mod. Phys. A* **24**, 5925 (2009).
- [10] B. Paczynski, *Acta Astron.* **42**, 145 (1992); C. Thompson and R. C. Duncan, *ApJ.* **392**, L9 (1992); **473**, 322 (1996); A. Melatos, *Astrophys. J. Lett.* **519**, L77 (1999).
- [11] L. Dong and S. L. Shapiro, *ApJ.* **383**, 745 (1991); M. Bocquet, S. Bonazzola, E. Gourgoulhon, and J. Novak, *Astron. Astrophys.* **301**, 757 (1995).
- [12] E. J. Ferrer, V. de la Incera, J. P. Keith, I. Portillo and P. L. Springsteen, *Phys. Rev. C* **82**, 065802 (2010); L. Paulucci, E. J. Ferrer, V. de la Incera, and J. E. Horvath, *Phys. Rev. D* **83**, 043009 (2011).



- [13] K. G. Klimenko, *Teor. Mat. Fiz.* **90**, 3 (1992); V. P. Gusynin, V. A. Miransky and I. A. Shovkovy, *Phys. Rev. Lett.* **73**, 3499 (1994); *Phys. Lett. B* **349**, 477 (1995); *Nucl. Phys.* **B563**, 361 (1999).
- [14] C. N. Leung, Y. J. Ng and A. W. Ackley, *Phys. Rev. D* **54**, 4181(1996); E. J. Ferrer and V. de la Incera, *Phys. Rev. D* **58**, 065008 (1998); E. J. Ferrer and V. de la Incera, *Phys. Lett. B* **481**, 287 (2000); Yu. I. Shilnov, and V. V. Chitov, *Phys. Atom. Nucl.* **64** (2001) 2051; N. Sadooghi, A. Sodeiri Jalili, *Phys. Rev. D* **76**, 065013 (2007); E. Rojas, A. Ayala, A. Bashir, and A. Raya, *Phys. Rev. D* **77**, 093004. (2008); A. Raya and E. Reyes. *Phys. Rev. D* **82** 016004 (2010).
- [15] E. Elizalde, E. J. Ferrer, and V. de la Incera, *Phys. Rev. D* **68**, 096004 (2003).
- [16] C. N. Leung and S.-Y. Wang, *Nucl. Phys.* **B747**, 266 (2006).
- [17] E. J. Ferrer, V. de la Incera and A. Sanchez. *Phys. Rev. Lett.* **107**, 041602 (2011); *Nucl. Phys.* **864**, 469 (2012).
- [18] D.-S Lee, C. N. Leung and Y. J. Ng, *Phys. Rev. D* **55**, 6504 (1997); E. J. Ferrer, and V. de la Incera, *Phys. Rev. D* **58**, 065008 (1998); *Phys. Lett. B* **481**, 287 (2000); E. Elizalde, E. J. Ferrer, and V. de la Incera, *Phys. Rev. D* **68**, 096004 (2003); E. Rojas, A. Ayala, A. Bashir, and A. Raya, *Phys. Rev. D* **77**, 093004 (2008); E. J. Ferrer, and V. de la Incera, *Phys. Rev. Lett.* **102**, 050402 (2009);
- [19] E. J. Ferrer and V. de la Incera, *Phys. Rev. Lett.* **102**, 050402 (2009); *Nucl. Phys.* **B824**, 217 (2010).
- [20] S. Frautschi, *in: Proceedings of the Workshop on Hadronic Matter at Extreme Energy Density*, N. Cabibbo, ed. (Erice, Italy 1978); B. C. Barrois, *Nucl. Phys.* **B129**, 390 (1977); D. Bailin and A. Love, *Phys. Rep.* **107**, 325 (1984).
- [21] M. Alford, C. Kouvaris, and K. Rajagopal, *Phys. Rev. Lett. B* **92**, 222001 (2004); *Phys. Rev. D* **71**, 054009 (2005).

- [22] R. Casalbuoni, R. Gatto, M. Mannarelli, G. Nardulli and M. Ruggieri, Phys. Lett. B **605**, 362 (2005) [Erratum-ibid B615 (2005) 297]; M. Alford, and Q. Wang, J. Phys. G **31**, 719 (2005); K. Fukushima, Phys. Rev. D **72**, 074002 (2005).
- [23] P. F. Bedaque and T. Schafer, Nucl. Phys. **A697**, 802 (2002); A. Kryjevski and T. Schafer, Phys. Lett. B **606**, 52 (2005); A. Gerhold and T. Schafer, Phys. Rev. D **73**, 125022 (2006).
- [24] M. Alford, J. A. Bowers, and K. Rajagopal, Phys. Rev. D **63**, 074016 (2001); I. Giannakis and H. C. Ren, Phys. Lett. B **611**, 137 (2005); Nucl. Phys. **B723**, 255 (2005); R. Casalbuoni, *et. al*, Phys. Lett. B **627**, 89 (2005); M. Ciminale, G. Nardulli, M. Ruggieri and R. Gatto, Phys. Lett. B **636**, 317 (2006); K. Rajagopal and R. Sharma, Phys. Rev. D **74**, 094019 (2006).
- [25] E. J. Ferrer and V. de la Incera, Phys. Rev. Lett. **97**, 122301 (2006); Phys. Rev. D **76**, 114012 (2007); J. Phys. A **40**, 6913 (2007).
- [26] S. B. Rüster, *et al.*, Phys. Rev. D **72**, 034004 (2005).
- [27] M. Kitazawa, D. H. Rischke and I. A. Shovkovy, Phys. Lett. B **637**, 367 (2006); H. Abuki and T. Kunihiro, Nucl. Phys. A **768**, 118 (2006).
- [28] M. Matsuzaki, Phys. Rev. D **62**, 017501 (2000); H. Abuki, T. Hatsuda and K. Itakura, Phys. Rev. D **65**, 074014 (2002); K. Itakura, Nucl. Phys. **A715**, 859 (2003).
- [29] D. M. Eagles, Phys. Rev. **186**, 45 (1969); A. J. Leggett, J. Phys. **41**, C7 (1980); P. Nozières and S. Sachmitt-Rink, J. Low Temp. Phys. **59**, 195 (1985); Q. Chen, J. Stalic, S. Tan and K. Levin, Phys. Rep. **412**, 195 (2005); H. Stein, *et. al*, Z. Phys. **A351**, 295 (1995); U. Lombardo, P. Nozieres, P. Schuck, H. J. Schulze and A. Sedrakian, Phys. Rev. C **64**, 064314 (2001).
- [30] Y. Nishida and H. Abuki, Phys. Rev. D **72** (2005) 096004; L. He and P. Zhuang, Phys. Rev. D **75** (2007) 096003; **76** (2007) 056003.

- [31] A. H. Rezaeian, H. J. Pirner, Nucl. Phys. **A779**, 197 (2006); L. He and P. Zhuang, Phys. Rev. D **76**, 056003 (2007); G.-F. Sun, L. He, and P. Zhuang, Phys. Rev. D **75**, 096004 (2007); H. Abuki, Nucl. Phys. **A791**, 117 (2007); M. Kitazawa, D. H. Rischke and I. A. Shovkovy, Phys. Lett. B **663**, 228 (2008); H. Abuki and T. Brauner, Phys. Rev. D **78**, 125010 (2008); J. Deng, J.-C. Wang and Q. Wang, Phys. Rev. D **78**, 034014 (2008); D. Blaschke, and D. Zablocki, Phys. Part. Nucl. **39**, 1010 (2008); T. Brauner, Phys. Rev. D **77**, 096006 (2008); J. O. Andersen, Nucl. Phys. **A820**, 171C (2009); H. Guo, C.-C. Chien, and Y. He, Nucl. Phys. **A823**, 83 (2009); B. Chatterjee, H. Mishra, and A. Mishra, Phys. Rev. D **79**, 014003 (2009); T. Hatsuda, M. Tachibana, N. Yamamoto and G. Baym, Phys. Rev. Lett. **97**, 122001 (2006); N. Yamamoto *et al.*, Phys. Rev. D **76**, 074001 (2007); T. Hatsuda, M. Tachibana, and N. Yamamoto, Phys. Rev. D **78**, 011501 (2008); N. Yamamoto and T. Kanazawa, Phys. Rev. Lett. **103**, 032001 (2009); J. Deng, A. Schmitt and Q. Wang, Phys. Rev. D **76**, 034013 (2007); H. Basler and M. Buballa, Phys. Rev. D **82**, 094004 (2010); J.-C. Wang, Q. Wang, and D. H. Rischke, Phys. Lett. B **704**, 347 (2011).
- [32] J. C. Wang, V. de la Incera, E. J. Ferrer, Q. Wang, Phys. Rev. D **84**, 065014 (2011).
- [33] H. Abuki, G. Baym, T. Hatsuda and N. Yamamoto, Phys. Rev. D **81**, 125010 (2010).
- [34] E. J. Ferrer and J. P. Keith Phys. Rev. C **86**, 035205 (2012).
- [35] F. Wilczek, *Diquarks as Inspirations and as Objects*, Ian Kogan Memorial volume, ed. M. Shifman. Ann Arbor 2004, Deserfest, 322-338 (hep-ph/0409168).
- [36] M. Alford and S. Reddy, Phys. Rev. D **67**, 074024 (2003).
- [37] S. P. Klevansky and R. H. Lemmer, Phys. Rev. D **39**, 3478 (1989);
- [38] D. Ebert and M. K. Volkov, Phys. Lett. B **272**, 86 (1991); S. P. Klevansky, Rev. Mod. Phys. **64**, 649 (1992); I. V. Krive and S. A. Naftulin, Phys. Rev. D **46**, 2737 (1992); K. G. Klimenko, Z. Phys. C **54**, 323 (1992); V. P. Gusynin, V. A. Miransky and

- I. A. Shovkovy, Phys. Lett. B **349**, 477 (1995); I. Shushpanov and A. V. Smilga, Phys. Lett. B **402**, 351 (1997); A. Yu. Babansky, E. V. Gorbar, and G. V. Shchepanyuk, Phys. Lett. B **419**, 272 (1998); D. Ebert, K. G. Klimenko, M. A. Vdovichenko, and A. S. Vshivtsev, Phys. Rev. D **61**, 025005 (1999); N. O. Agasian and I. A. Shushpanov, Phys. Lett. B **472**, 143 (2000); V. C. Zhukovsky, *et. al*, JETP Lett. **74**, 523 (2001); D. Kabat, K. Lee, and E. Weinberg, Phys. Rev. D **66**, 014004 (2002); E. S. Fraga and A. J. Mizher, Phys. Rev. D **78**, 025016 (2008); A. J. Mizher, M. N. Chernodub, E. S. Fraga, Phys. Rev. D **82**, 105016 (2010); P. Watson and H. Reinhardt, arXiv:1310:6050 [hep-ph].
- [39] E. J. Ferrer, V. de la Incera, I. Portillo, and M. Quiroz, Phys. Rev. D **89**, 085034 (2014).
- [40] B. Feng, E. J. Ferrer and V. de la Incera, Nucl. Phys. **B853**, 213 (2011); Phys. Lett. B **706**, 232 (2011).
- [41] S. Klimt, M. Lutz and W. Weise, Phys. Lett. B **249**, 386 (1990).
- [42] M. Kitasawa, T. Koide, T. Kunihiro, and Y. Nemoto, Prog. Theor. Phys. **108**, 929 (2002).
- [43] B. Feng, E. J. Ferrer and V. de la Incera, arXiv:1304.0256 [nucl-th].
- [44] V. I. Ritus, Ann. Phys. **69**, 555 (1972); Sov. Phys. JETP **48**, 788 (1978) [Zh. Eksp. Teor. Fiz. 75, 1560 (1978)]; E. Elizalde, E. J. Ferrer, and V. de la Incera, Ann. of Phys. **295**, 33 (2002); Phys. Rev. D **70**, 043012 (2004); G. Murguia, A. Raya, A. Sanchez, E. Reyes, Am. J. Phys. **78**, 700 (2010).
- [45] E. J. Ferrer, V. de la Incera and C. Manuel, Phys. Rev. Lett. **95**, 152002 (2005); Nucl. Phys. **B747**, 88 (2006).
- [46] B. L. Ioffe and A. V. Smilga, Nucl. Phys. **232**, 109 (1984).

- [47] J. Schwinger, Phys. Rev. **73**, 416 (1947).
- [48] B. Jancovici Phys. Rev. A **187**, 2275 (1969); E. J. Ferrer, V de la Incera, D. Manreza Paret, A. Prez Martnez; *"Anomalous-Magnetic-Moment Effects in a Strongly Magnetized and Dense Medium"* in the electronic proceedings of the conference: *Compact Stars in the QCD Phase Diagram III (CSQCD III)*, Guaruj, SP, Brazil (arXiv:1307.5947 [nucl-th]).
- [49] P. Rehberg, S. P. Klevansky and J. Hüfner, Phys. Rev. C **53**, 410 (1996).
- [50] J. I. Kapusta, *Finite-Temperature Field Theory*, Cambridge Univ. Press, Cambridge 1989.
- [51] V. P. Gusynin and I. A. Shovkovy, Phys. Rev. D **56**, 5251 (1997).
- [52] G. S. Bali, *et. al*, Phys. Rev. D **86**, 094512 (2012).
- [53] E. J. Ferrer, V. de la Incera, J. P. Keith, I. Portillo, arXiv:1405.7422v2 [hep-ph]
- [54] Y. Nishida and H. Abuki, Phys. Rev. D **72**, 096004 (2005).
- [55] L. He and P. Zhuang, Phys. Rev. D **75**, 096003 (2007).
- [56] A. A. Osipov, B. Hiller and J. da Providencia, Phys. Lett. B **634**, 48 (2006).
- [57] J. F. Donoghue and K. S. Sateesh, Phys. Rev. D **38**, 360 (1988).
- [58] D. Kastor and J. Traschen, Phys. Rev. D **44**, 3791 (1991); J. E. Horvath, J. A. de Freitas Pacheco, and J. C. N. de Araujo, Phys. Rev. D **46**, 4754 (1992); J. E. Horvath, G. Lugones, and J. A. Freitas Pacheco, Int. J. Mod. Phys. D **12**, 519 (2003); A. H. Rezaeian and H. J. Pirner, Nucl. Phys. A **779**, 197 (2006); A. K. Sisodiya, R. S. Kaushal, D. Parashar, and V. S. Bhasin, J. Phys. G **32**, 1193 (2006); **34**, 929 (2007).
- [59] H. E. Haber and H. A. Weldon, Phys. Rev. Lett. **46**, 1497 (1981).

- [60] J. A. Wheeler, Phys. Rev. **97**, 511 (1955).
- [61] I. Shovkovy, Found. Phys. **35**, 130 (2005); M. Huang, I. Shovkovy, Nucl. Phys. **A729**, 835 (2005).
- [62] D. Kincaid and W. Cheney, *Numerical Analysis*, (3er ed. 2002)
- [63] J. Nocedal and S. J. Wright, *Numerical Optimization*, (2nd ed. 2006)
- [64] J. E. Dennis and R. B. Schnabel, *Numerical Methods for Unconstrained Optimization and Nonlinear Equations* , (1996)
- [65] I. E. Frolov, V. Vh. Zhukovsy, and K. G. Klimenco, Phys. Rev. D **82**, 076002 (2010).

# Curriculum Vitae

Israel Portillo Vazquez was born in Hidalgo del Parral, Chihuahua, Mexico. In June, 2008, Israel obtained his bachelor degree in Electronic Engineering at the Instituto Tecnológico de Chihuahua, in Chihuahua, Chihuahua, Mexico. From January of 2009 to June 2011, Israel studied a MS in Physics at the University of Texas at El Paso (UTEP). During this time, Israel worked in collaboration with the theoretical-high-energy-physics group at UTEP headed by Dr. Efrain Ferrer and Dr. Vivian Incera. In May 2011, Israel was honored by the Physics Department at UTEP for his outstanding research work. Israel continues his Ph. D. studies at UTEP in the Computational Science Program (CPS), where now, with the defence of this dissertation, is obtaining his Ph. D. degree.

Permanent address: 1265 Doy Dr.

El Paso, Texas 79928

This thesis was typed by Israel Portillo Vazquez.